Empirical Closures for Momentum and Energy Transport in Hall Thrusters based on Thomson Scattering Measurements

IEPC-2024-393

Presented at the 38th International Electric Propulsion Conference, Toulouse, France
June 23-28, 2024

Parker J. Roberts,[*] Madison G. Allen,[†] Declan G. Brick,[‡] and Benjamin A. Jorns[§]
University of Michigan, Ann Arbor, Michigan, 48109, U.S.A.

Non-classical contributions to the electron momentum and energy balance in the Hall thruster acceleration region are characterized non-invasively for various propellants and operating conditions. Incoherent Thomson scattering and laser-induced fluorescence are combined to determine the electron and ion properties throughout the near-field plume of a magnetically shielded, laboratory Hall thruster. The thruster is operated on both xenon and krypton propellant at multiple discharge currents and voltages. The inverse Hall parameter, which parameterizes the anomalous electron momentum transport, is estimated directly from these data based on a 1D Ohm's law approximation for the electron and ion flow on channel centerline of the thruster which accounts for multiple ionization. It is found that the peak electron temperatures exceed 20% of the discharge voltage, in contrast with the traditional scaling law of 10% in unshielded Hall thrusters. Further, the acceleration zone is found to shift axially with the electric field at different operating conditions, as evidenced by the profiles of temperature, electric field, and total collision frequency. Based on a fit to this dataset, an empirical scaling for closure models for the anomalous crossed-field transport is presented and discussed. Following this 1D analysis, a two-dimensional map of the electron properties in the thruster plume is also performed in order to assess the transport of heat by electrons both perpendicular and parallel to the magnetic field. It is found that the electron temperature varies significantly along field lines, with electrons on channel centerline reaching large peak temperatures exceeding 60 eV, but cooling to below 20 eV at the plume edges. In response to this result, a framework for approximating the electron energy transport as a polytropic expansion law along field lines is discussed in terms of the full fluid energy equation. Qualitative agreement is found with fluid simulations that assume reduced parallel-field heat fluxes, suggesting that electron heat transport cannot be accurately described by classical, local formulations.

---

[*] Doctoral Candidate, Department of Aerospace Engineering, pjrob@umich.edu
[†] Doctoral Candidate, Department of Aerospace Engineering, mgallen@umich.edu
[‡] Doctoral Candidate, Department of Aerospace Engineering, brickd@umich.edu
[§] Associate Professor, Department of Aerospace Engineering, bjorns@umich.edu

I. Introduction

The Hall thruster is a pivotal propulsion technology for efficiently maneuvering in both Earth orbit and deep space, which stems from its ability to provide high thrust and specific impulse relative to other electric propulsion systems. These devices accomplish this with a crossed-field, partially magnetized plasma channel that efficiently ionizes and accelerates propellant through a quasineutral electric field.[1,2] Despite the promising performance and substantial flight heritage of Hall thrusters, aspects of their operation remain poorly understood. Capturing these complex discharge physics with models is essential for the accurate prediction of operation in untested situations, for example to project ground test data to orbital performance and to validate and qualify new designs.[3]

A key challenge for modeling Hall thrusters is the "anomalous" transport of heat and momentum by electrons,[4,5] which is widely thought to be due to nonlinear effects from kinetic plasma turbulence.[6] However, the precise dependence of the non-classical heat and momentum flux on the plasma properties, which is necessary to close the equations for a fluid description of the electrons, remains elusive. This anomalous transport directly impacts nearly every aspect of Hall thruster operation, including thrust efficiency,[7] body heating,[8] and the electric field profile,[2,9] which in turn determines surface erosion and lifetime.[10,11]

The unknown scaling of this non-classsical transport also poses difficulties for efforts to predictively model how thruster performance will depend on changes to design geometries, operating conditions, or differences between test facilities and operation on orbit.[12] Additionally, the particular scaling of the anomalous electron momentum transport with discharge current determines the theoretical upper limit on thrust density for these devices, and the uncertainty in the nature of this scaling to date leaves an order of magnitude range of possible optimum performance.[13] To this end, global efficiency measurements of Hall thrusters operating at high currents recently showed experimentally that thruster efficiency at high powers is principally limited by decreases in electron confinement and ion beam divergence.[14] Both of these factors result directly from changes in the electron dynamics.

To address these challenges, recent independent investigations using incoherent Thomson scattering diagnostics revealed unexpectedly high electron temperatures in the plumes of magnetically shielded Hall thrusters[15,16] relative to fluid model predictions and Langmuir probe measurements.[17,18] This finding suggests that the widely used methods for describing electron heat transport in these models need revision, as the observed temperatures indicate that thermal flux is not accurately captured by existing assumptions.[19] Moreover, because momentum transport is coupled to heat transport via the pressure gradient force, these findings imply broader implications for our understanding of electron motion in Hall thrusters including the ability to model ion trajectories and erosion.

Preliminary fluid modeling efforts incorporating alternate assumptions about anomalous heat transport have aligned with the observed temperatures at a single operating condition, as presented in an accompanying work[20]; however, important questions remain. In particular, these findings raise the issue of how the anomalous electron momentum transport profile varies with discharge current, voltage, and propellant type. By compiling this data, it may be possible to identify patterns which govern the anomalous electron transport as a function of local plasma properties - if a general function could be found, this would "close" the fluid equations and allow self-consistent models. Additionally, does the finding that a large amount of heat is being trapped within the electron population along the center of the thruster channel necessitate modifications to the energy equation only as a cross-field effect, or also along magnetic field lines? It is therefore crucial to investigate the scaling of electron properties in the Hall thruster plume across multiple operating conditions, as well as to assess the validity of the assumption that the magnetic field lines are isothermal, with non-intrusive measurements.

In this work, we address these questions by performing incoherent Thomson scattering (ITS) measurements on a laboratory Hall thruster while varying the discharge current, discharge voltage, and propellant. By combining these electron property measurements with Laser-Induced Fluorescence (LIF) measurements of ion properties, we enable the regression of models for fluid parameters which quantify the anomalous transport of both heat and momentum in the acceleration region of the Hall thruster. We also present a 2D ITS map of the electron temperature and density in the near-field plume. This provides the ability to measure electron properties relative to the magnetic field geometry, which allows direct assessment of the approximations for electron energy flow used to model electrons as a fluid.

This paper is structured as follows: Section II discusses the theoretical principles underlying the current understanding of anomalous electron momentum and heat transport. Section III details the experimental apparatus used for incoherent Thomson scattering and laser-induced fluorescence. Section IV then presents the experimental results obtained under varied thruster operating conditions and includes a 2D mapping of electron properties in the plume. Following this, Section V puts these results in context by examining the scaling of the non-classical transport with fluid plasma parameters. In this section, we present a closure model that describes the scaling of the anomalous transport at all tested operating conditions, and propose a polytropic description of the electron expansion along field lines. Finally, Section VI summarizes the key findings and conclusions of the study, while Appendix A. details the Bayesian sampling algorithm employed to characterize fluid properties under diagnostic uncertainty.

II. Anomalous Electron Transport of Fluid Properties

In this section, we provide a brief overview of the operating physics of a Hall thruster discharge, based on a 1D, Ohm's Law-based model for the electron force balance. We discuss the use of this model to infer the anomalous collision frequency from laser diagnostic measurements. Following this, we discuss the electron energy equation, including the nature of 2D energy flow in the axial-radial plane. We introduce the local polytropic index, γ, as a convenient parameter for representing the non-classical electron energy flow along field lines.

A. Electron Momentum Transport

A Hall thruster, shown in Fig. 1, consists of an annular plasma channel with an internal ring anode. The thermionic hollow cathode located outside of the channel emits electrons and establishes a potential difference relative to the anode. As the electrons migrate toward the anode, a strong radial magnetic field restricts their motion. This field leads to increased resistivity, which Ohmically heats the electrons to temperatures at which they begin to ionize neutral propellant injected from the anode. This increased resistivity also localizes the electric field to the region of large magnetic field, forming an "acceleration zone" within which the newly formed ions are accelerated and ejected, producing thrust. To maintain quasineutrality, an equal current of electrons from the cathode join the ejected ions to form the beam.

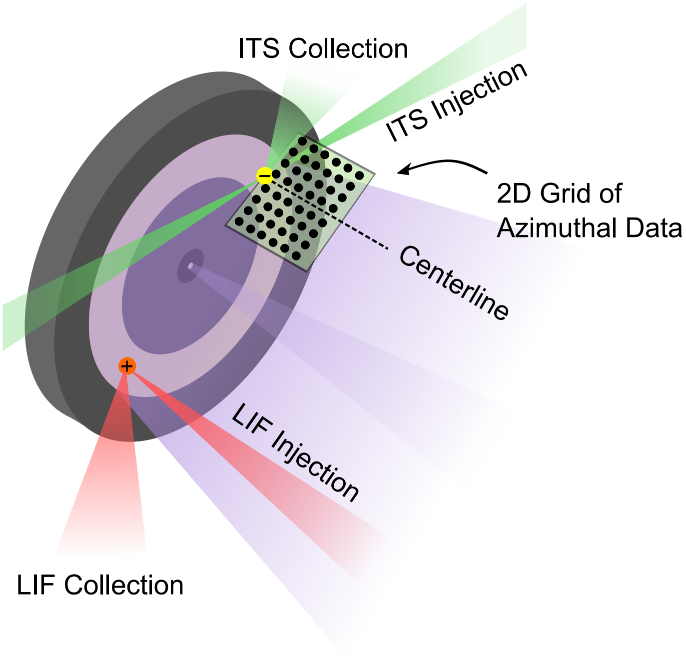

Figure 1. Diagram of the H9 thruster plume, with laser diagnostic injection axes overlaid

The local electron motion can be quantified with a simplified Ohm's law description of the plasma.[1] To obtain this, we use a fluid momentum conservation equation for the electrons. By assuming that the electron inertia is negligibly small, we arrive at the relationship

$$0 = -en_e\vec{E} - en_e\vec{u}_e \times \vec{B} - \nabla p_e - m_e n_e \nu_e \vec{u}_e. \tag{1}$$

This expression describes an equilibrium balancing the force on the electrons from the electric field, E, with that of the magnetic field, $\vec{B}$, in addition to the gradient in electron pressure p_e. The final term accounts for the loss of bulk fluid momentum to collisions with other species (ions and neutrals) at a rate ν_e. In this formulation, we have ignored the ion velocity contribution to the collisional drag term for electron-ion collisions. On the channel center line of the thruster in the near field plume, the electric field is nearly axial, $\vec{E} \approx E_z\hat{z}$, and the magnetic field is nearly radial, $\vec{B} \approx B_r\hat{r}$. Under these conditions, we can solve Eq. 1 for the electron velocities,

$$\begin{aligned} u_{e\phi} &= \frac{1}{\Omega^{-2}+1}\left(u_{E\times B} + u_{\nabla p}\right), \\ u_{ez} &= -\frac{\Omega^{-1}}{\Omega^{-2}+1}\left(u_{E\times B} + u_{\nabla p}\right), \end{aligned} \tag{2}$$

where the $E \times B$ drift speed is $u_{E\times B} = E_z/B_r$, the diamagnetic drift speed is $u_{\nabla p} = \partial_z p_e/(en_eB_r)$, and the Hall parameter is $\Omega = eB_r/(m_e\nu_e)$, with e being the electron charge magnitude and m_e being the electron mass. Equation 2 demonstrates that in absence of collisions ($\Omega \gg 1$), the azimuthal drift is the sum of the single-particle drifts. However, when the collision rate increases, Ω decreases and a portion of this drift energy is redirected into the axial direction.

In principle, the total momentum-loss electron collision rate ν_e can be computed from the local plasma properties as the sum of the classical rates for electron-neutral and electron-ion collisions, for example based on tabulated cross sections and Rutherford scattering. Experimentally, however, Hall thrusters generally exhibit orders of magnitude higher cross-field current than would be expected from this classical calculation.[4,21] This phenomenon corresponds directly to an anomalously large u_{ez} in Eq. 2. This enhanced cross-field current is thought to be associated with an effective drag force on the electrons caused by interactions with microscopic plasma instabilities,[22] which could only be captured directly in expensive, kinetic modeling frameworks. However, this behavior can be parametrically represented in fluid modeling equations by adding an anomalous collision frequency to the classical value, i.e. $\nu_e = \nu_{\text{class}} + \nu_{\text{AN}}$.

In this work, we follow the recently developed experimental framework for determining ν_e from non-invasive, experimental measurements in Ref. 16, in the form of the dimensionless inverse Hall parameter, Ω^{-1}. Namely, we solve Eq. 2 for this quantity, yielding

$$\Omega^{-1} = \frac{-2u_{ez}/u_{\text{drift}}}{\left(1 + \sqrt{1 + 4u_{ez}/u_{\text{drift}}}\right)}, \tag{3}$$

where $u_{\text{drift}} = (u_{E\times B} + u_{\nabla p})$. Therefore, provided that we can measure the quantities E_z, B_r, u_{ez}, and $p_e = n_e k_B T_e$ for the Boltzmann constant k_B, we can infer the local inverse Hall parameter from experimental measurements. Measuring Ω^{-1} experimentally in this way provides a macroscopic metric which can be directly implemented to calibrate fluid Hall thruster simulations, as well as used for the purpose of building up a training dataset of anomalous transport properties from which to regress first-principles and data-driven closure models.

In a 1D approximation of the plasma properties on channel center line, the electric field can be determined from laser-induced fluorescence measurements (LIF), while n_e and T_e are directly observable with incoherent Thomson scattering. However, the time-averaged cross-field drift velocity, u_{ez}, is more difficult to infer from a measured EVDF due to its small value relative to the spread of the electron distribution ($u_{ez}/v_{Te} \sim 10^{-3}$). In principle, within a one-dimensional approximation, u_{ez} can be estimated from the known discharge current given the Hall thruster channel area; however, this approach would fail to account for any variation in plasma density and electron velocity off of centerline. Instead, to estimate this quantity on centerline, we rely on a current conservation argument to infer u_{ez} from downstream probe measurements from a previous study, while accounting for the prescence of multiply charged ions. For a steady state flow, charge continuity guarantees that

$$\nabla \cdot \vec{J} = \nabla \cdot \left(\vec{J}_e + \vec{J}_i\right) = 0, \tag{4}$$

where $\vec{J}$ is the total current density and $\vec{J}_e$ and $\vec{J}_i$ are the electron and ion current densities, respectively. We approximate this relationship in the 1D sense by ignoring the effects of divergence, charge-exchange collisions, and ionization, making the assumption that $\partial \vec{J}/\partial r$ vanishes. The azimuthal component of the derivative must also vanish by axisymmetry of the Hall thruster. This results in the finding that the total axial current density, J_z, is constant through the plume. In a previous study on this thruster, we leveraged far-field current-collecting probes to characterize the so-called beam utilization efficiency $\eta_B = J_i/(J_i + J_e)$, defined as the ratio of ion current to total current. While our inference of J_z is primarily based on local measurements, it does rely on the assumption that this ion current density fraction which we measure in the far-field plume applies locally as well. We also applied a Wein filter to characterize the current fraction, $\omega_Z = J_Z/J_i$, of each ion charge state Z, for $Z \leq 3$ (higher charge states are not present to a significant extent in this work). Because we are ignoring the effects of ionization, the current density of each charge state is constant through the plume, e.g. $J_{iZ} = Zen_{iZ}(z)u_{iZ}(z)$. Given this information, we can solve for the axial electron velocity as

$$u_{ez}(z) = -\frac{J_e}{en_e(z)} = \frac{J_1 + J_2 + J_3}{en_e(z)}\left(1 - \frac{1}{\eta_B}\right). \tag{5}$$

The respective ion charge state current densities can be determined by invoking the principle of quasineutrality, i.e. $n_e \approx n_1 + 2n_2 + 3n_3$, to yield the expressions

$$J_1 = en_e u_1\left(1 + \frac{2}{\sqrt{2}}\frac{\omega_2}{\omega_1} + \frac{3}{\sqrt{3}}\frac{\omega_3}{\omega_1}\right)^{-1}, \tag{6}$$

$$J_2 = \frac{\omega_2}{\omega_1}J_1, \tag{7}$$

$$J_3 = \frac{\omega_3}{\omega_1}J_1. \tag{8}$$

While this formulation is somewhat crude in that it does not account for important effects such as ionization and divergence, this framework provides a simple analytical method for estimating the shape of the anomalous collision frequency profile directly from non-invasive measurements on channel centerline.

B. Electron Energy Transport

In addition to the momentum conservation, it is crucial to correctly model the next-highest velocity moment of the electron kinetics: the internal energy. The conservation of energy by electrons can be described for an isotropic plasma by a simplified fluid pressure evolution equation, of the form

$$\frac{3}{2}\frac{\partial p_e}{\partial t} + \frac{5}{2}\nabla \cdot (p_e \vec{u}_e) = \vec{E} \cdot \vec{J} - \nabla \cdot \vec{q}_e. \tag{9}$$

In this expression, the two terms on the left hand side represent the variation of the pressure, and therefore of the internal energy, with time and space. On the right hand side, the first term corresponds to classical "Ohmic" heating. The second term represents the energy flow due to the internal heat flux, $\vec{q}_e$. This term arises from skew (the third velocity moment) of the distribution function, and represents the heat flow within the fluid frame of reference. In this work, we neglect interactions with other species, such as ionization and classical frictional heating, which would also contribute as sources and/or sinks to the RHS of Eq. 9, for the purpose of illustration. Based on this formulation, we seek to capture the behavior of missing terms in Eq. 9, which correspond in reality to any non-classical turbulent heating effects, by inferring an effective heat flux, $\vec{q}$.

For a magnetized plasma it is convenient to define a coordinate system aligned with the magnetic field lines. We can define corresponding heat flux vectors, $\vec{q}_\perp$ and $\vec{q}_\parallel$. If the plasma is sufficiently collisional, it is typical to represent the heat flux as a Fourier law with the Spitzer-Harm thermal conductivity, i.e.

$$\vec{q}_{e,SH} = -\kappa \nabla T_e, \tag{10}$$

where κ is a fluid transport parameter representing the thermal conductivity. Indeed, based on the classical electron-ion collision time[23],

$$\tau_{ei} = \frac{6\sqrt{2}\pi^{3/2}\epsilon_0^2\sqrt{m_e}(k_B T_e)^{3/2}}{\ln \Lambda e^4 n_e}, \tag{11}$$

where ϵ_0 is the vacuum permittivity, m_e is the electron mass, and $\ln\Lambda$ is the Coulomb logarithm, the closed-form Chapman-Enskogg expansion of the moment equations yields Fourier heat flux scaling with a parallel thermal conductivity,

$$\kappa_{\|} \approx 3.2\frac{n_E \tau_{ei} k_B T_e}{m_e}, \tag{12}$$

and the perpendicular thermal conductivity,

$$\kappa_{\perp} \approx 4.7\frac{n_e k_B T_e}{m_e \omega_{ce}^2 \tau_{ei}}. \tag{13}$$

This Fourier scaling leads to classical heat diffusion behavior, characterized by the smoothing out of localized peaks in temperature. We ignore here an additional term in the Braginskii formulation[23,24] which accounts for flow of electron current along magnetic field lines, which we expect to be small. Note that for strongly magnetized electrons ($\Omega >> 1$) which are still collisional enough that these expressions apply, the dependence on ω_{ce} reduces the heat flux perpendicular to field lines relative to the heat flux parallel to field lines, for similar thermal gradients.

Models for electron physics often adopt these approximations but calculate κ based on the total collision frequency, ν_e, which was used to represent kinetic bulk momentum transfer in Eq. 1.[25] Other leading models simply assume that the electron temperature is constant along magnetic streamlines.[26] However, because the effective collision rate is an approximation for kinetic momentum transfer, for example due to plasma wave field forces, this framework is not in general predictive of the impact of these non-classical interactions on energy transport. More generally, then, $\vec{q}_e$ may deviate significantly from Fourier-like scaling in the presence of plasma instabilities, as shown in numerical systems and previous studies of Hall thrusters,[19] magnetic nozzle plasmas,[27] and fusion devices.[28] We previously investigated the electron energy transport properties with Thomson scattering studies along the Hall thruster channel centerline, in the cross-field direction.[19] This study made the key assumption that the heat flux along field lines was zero at the channel centerline, demonstrating that under this assumption, missing energy confinement across field lines must be accounted for. However, it remains to be seen how energy flows along field lines, and whether the anon-classical energy flow is primarily in the parallel or perpendicular direction, if not both.

In many plasma systems, it is common to adopt a polytropic law to describe the electron thermodynamics, of the form

$$T_e = c n_e^{\gamma-1}, \tag{14}$$

where γ is the polytropic index and c is a constant of proportionality. Equivalently, we can write this in terms of the pressure as $p_e = \alpha n e^{\gamma}$. This notation is inspired by the adiabatic limit: if $\vec{q}$ and $\vec{E}\cdot\vec{J}$ vanish, no heat is exchanged with the environment, and Eq. 9 reduces to Eq. 14 with $\gamma = 5/3$, for electrons in three dimensions.[29] In the opposite limit, if $\vec{q}$ is large enough along the expansion axis, heat flow via the internal heat flux dominates over convection (the LHS terms), and the plasma is isothermal ($\gamma = 1$). We adopt this framework in the following as a reference to describe the expansion of the plasma along magnetic field lines.

It is possible for γ to fall between the isothermal and adiabatic values (subadiabatic). For an expanding plasma, this corresponds to the temperature falling off more slowly with expansion than adiabatic scaling, meaning that some heat finite heat flux is important. The opposite situation is also possible. If the temperature falls off with density more rapidly than for adiabatic cooling, γ can exceed the adiabatic value (superadiabaticity), which corresponds to heating. By evaluating the behavior of the polytropic index, γ, along and perpendicular to field lines within the discharge, it is thus possible to characterize the nature of anomalous electron heating and cooling within the plasma. Ideally, the behavior of simplified parameters such as q or γ will provide an avenue to close the energy equation in fluid models for the electrons in a way that matches experimental data. In the following sections, we accomplish this by mapping the electron temperature and density throughout the Hall thruster plume in the r-z plane, and estimating γ along the magnetic field lines.

III. Methods

In this section, we discuss the details of our laser scattering experiment to infer the electron momentum and heat transport properties in the Hall thruster plume. We first cover the facility and laboratory Hall thruster, followed by an in-depth description of the ITS and LIF diagnostic apparatus and analysis procedures.

A. Thruster and Facility

In order to investigate the behavior of the anomalous transport profile with respect to global and local operational parameters of a Hall thruster, we performed a parametric study of the electron dynamics in a laboratory Hall thruster plume. The test article was the H9, a magnetically shielded, 9-kW class Hall thruster developed by the university of Michigan, the Air Force Research Laboratory (AFRL) and the Jet propulsion Laboratory (JPL).[30] The H9's shielded magnetic field shape, which is designed to prevent erosion of the thrsuter channel by ion sputtering, has the additional advantage of leading to a shift the acceleration region outside of the channel. This shift makes the region of electron heating and ion acceleration optically accessible for laser diagnostics. We tested the H9 in the Alec D. Gallimore Large Vacuum Test Facility (LVTF), a 6-meter-diameter, 9-meter long cylindrical vacuum chamber at the University of Michigan, at the operating conditions shown in Table 1.[31] We used a Stabil ion gauge to monitor the facility pressure, which was maintained at between 5 and 10 µTorr during thruster operation with a series of cryogenic pumps. We operated the H9 on both krypton and xenon propellant, at a range of discharge current values between 15 and 30 A, and a range of discharge voltage values between 300 and 600 V. These operating conditions were chosen to correpond to the conditions at which we previously acquired laser-induced fluorescence data, as reported in Ref. 32. In that work, the magnetic field strength was varied in order to minimize the intensity of the discharge current oscillations at each operating point. We electrically tied the thruster body to the cathode potential for this test.

Propellant	Discharge Voltage (V)	Discharge Current (A)	Magnetic Field (% Nominal)
Kr	300	15	100
Kr	300	30	87.5
Kr	400	15	112.5
Kr	600	15	112.5
Xe	300	15	100
Xe	300	30	100
Xe	600	15	100

Table 1. Operating conditions of the H9 thruster for which centerline measurements were taken.

B. Incoherent Thomson Scattering

To characterize the local plasma properties, we followed Ref. 16 in leveraging both incoherent Thomson scattering and laser-induced fluorescence velocimetry. The laser injection axes for these diagnostics is overlaid on Fig. 1, while Fig. 2 displays the full ITS injection apparatus. Thomson scattering is the process by which laser light inelastically scatters from electrons in the plasma. This diagnostic uses Doppler information encoded in this scattered spectrum to directly measure the time-averaged electron velocity distribution function along a particular axis. To accomplish this, our Thomson scattering apparatus relies on a Q-switched, frequency-doubled Nd:YAG laser with a wavelength of 532 nm. A beam expander telescope focuses this beam to a point within the thruster plume. After this, the beam enters the vacuum chamber through a v-coated window feedthrough, and is directed to the measurement location by a remotely steerable periscope within the chamber. The majority of the laser light passes through the thruster plume due to the low probability of scattering, and is collected by a water-cooled beam dump at the opposite chamber wall. However, a small number of photons within each laser pulse scatter from the electrons in the plasma. This scattered radiation is then collected by a 3-inch-diameter achromatic lens with a focal length of 200 mm, and then coupled to a 1-mm-diameter optical fiber which brings the scattered light to the collection bench.

The ITS collection bench is based on the approach of Vincent and Tsikata[33], and our implementation was previously validated in a hollow cathode plume in Ref. 34. This system collimates the scattered light launched from the fiber, which passes through a series of Volume Bragg Grating Notch Filters (VBG-BNFs); these are high-performance, narrow-bandwidth notch filters which, when aligned correctly, are capable of reducing the intensity of stray light at the laser wavelength so that the very weak Thomson broadening signal can be observed. After filtering, the light is re-focused into a triple-grating spectrometer. The diffracted spectrum then impinges upon the detector, which is made up of a 1024x1024 grid of electron multiplying and intensified charge-coupled device (EMICCD) pixels. Each column of pixels corresponds to a particular wavelength bin,

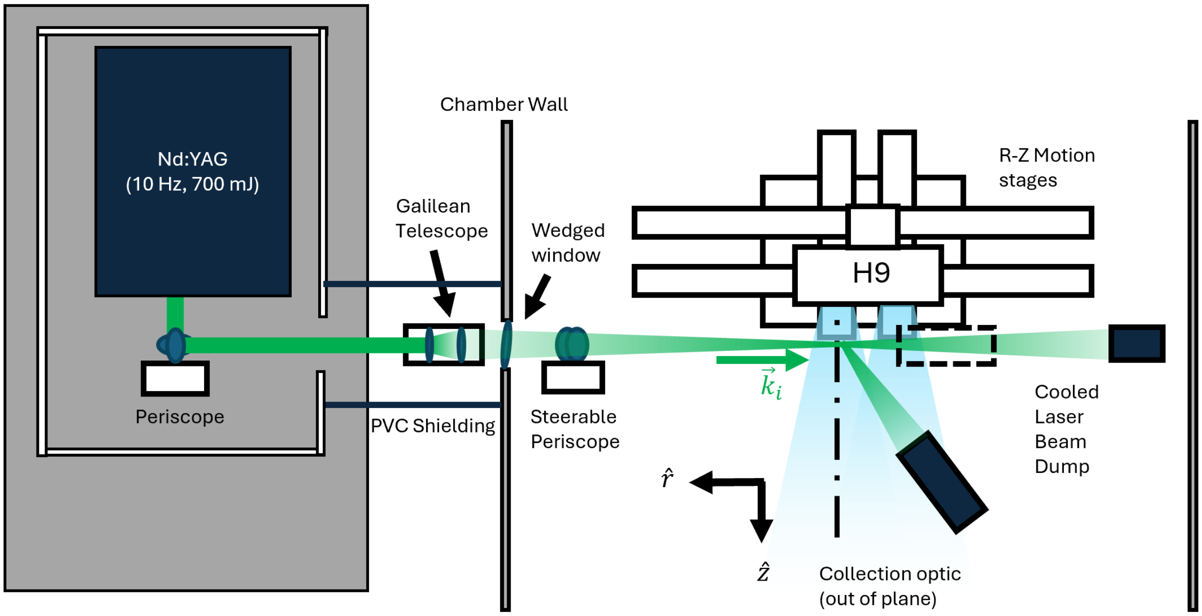

Figure 2. Schematic of the injection apparatus for Thomson scattering investigations of the H9 thruster plume. The collection optic is drawn out of the scattering plane, but in reality is located in the $r-\phi$ plane of the laser, pointed down at a 30° angle (dashed box).

while we average over the pixel rows which span the image of the optical fiber. This averaging is performed on the CCD itself ("hardware binning"), which reduces the background noise compared to performing the same process in software. The charge stored in each group of pixels is then digitized, resulting in a measure of the number of photon counts per wavelength bin per laser pulse; in other words, a measure of the wavelength spectrum of the light exiting the notch filters.

In most cases, the plasma background light intensity was intense compared to the Thomson scattering trace. For this reason, we acquired an equal number of plasma background acquisitions with the laser off, and subtracted these from the laser-on acquisitions. To accomplish this without taking additional experimental time, we programmed a function generator to trigger the EMICCD camera and acquire background shots in between laser pulses. We acquired for five minutes of experimental time at each position in the plume. This resulted in 6000 frames, with the even frames corresponding to 10-Hz laser-on data, and the odd frames corresponding to 10-Hz laser-off data delayed by 50 ms from the laser pulses. Since the laser pulse duration is on the order of 10 ns, there is little risk of reflections impacting the plasma-off shots with this acquisition regime. However, to increase signal to noise, it was necessary to ensemble average these 3000 laser-on and laser-off shots, resulting in an effectively time-averaged spectrum over the 5-minute acquisition window.

Figure 3 shows the background subtraction process for two locations and operating conditions. The background light from the plasma manifests as several rectangular peaks in the spectrum, which correspond to plasma emission lines broadened by the spectrometer instrument function. For the example trace with krypton propellant at 30 A discharge current, there is a clear and distinct difference between the laser-on and laser-off traces, and subtracting them results in a clear electron population which can be fit based on an equilibrium fluid approximation. However, as shown in Fig. 3(b), xenon plasmas generally have more intense optical emissions within the measurement bandwidth, and thus the Thomson spectrum is a smaller fraction of the background light. As a result, there is still a discernible peak when background subtraction is performed for xenon data, however the subtraction of these larger numbers results in increased noise in the subtracted trace. In a few cases with particularly large stray light from laser reflections on nearby surfaces, such as in the vicinity of the inner front pole, of the stray light spectrum is recorded separately with the thruster off, and is subtracted separately. These cases are discussed further in our companion work.[35]

As shown in Fig. 1, the incident ITS laser wavevector, $\vec{k}_i$, is horizontal. Meanwhile, scattered light impinges on the collection optic with wavevector $\vec{k}_s$, which lies at an angle $\theta = 30°$ from $\vec{k}_i$ in the same r-θ

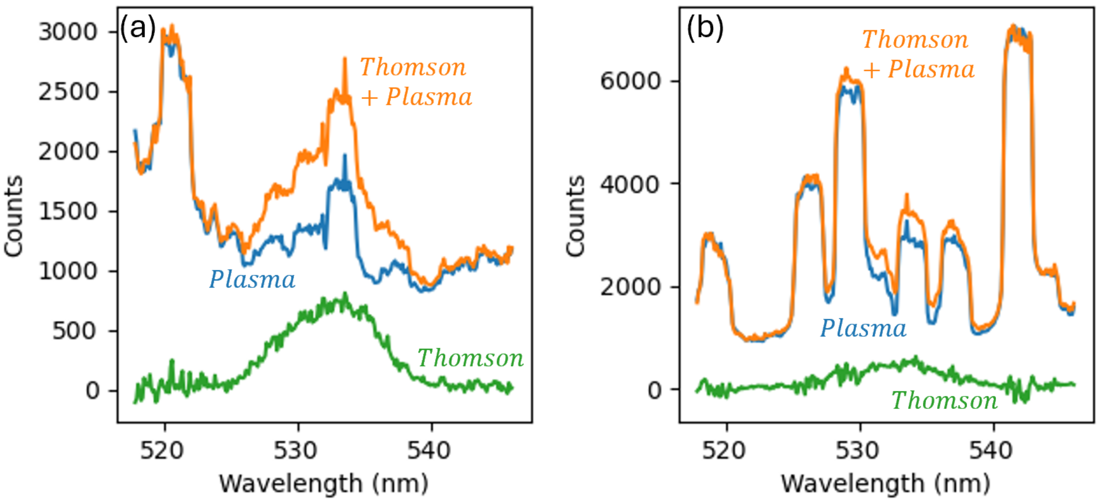

Figure 3. Examples of background subtraction for Thomson data. The orange curve shows the raw Thomson acquisition, while the blue curve shows the background plasma acquisition. The green curve is the difference of the two. (a) Krypton, 30 A. (b) Much brighter plasma emission from xenon at 15 A.

plane. The incoming laser light is polarized in the $\hat{z}$-direction, which maximizes the intensity of scattered light in the r-θ-plane. The difference between the two wavevectors, $\Delta\vec{k} = \vec{k}_s - \vec{k}_i$, determines the relationship between the scattered spectrum and the electron properties. In the limit that $\Delta k \lambda_D >> 1$, where $\lambda_D = \sqrt{k_B T_e/(n_e e^2)}$ is the Debye length of the plasma, the scattering is incoherent, meaning that phase correlations between light scattered off of nearby electrons are negligible. In the incoherent regime, the total scattered power is the independent sum of the power scattered from each individual electron. Since a photon scattered from a nonrelativistic electron with velocity $\vec{v}$ will experience a Doppler frequency shift

$$\Delta\omega = \vec{v} \cdot \Delta\vec{k}, \tag{15}$$

the intensity of the resulting spectrum at a frequency bin ω with width $d\omega$ is proportional to the number of electrons in the corresponding velocity bin $[v_k, v_k + dv_k]$, where $v_k = \vec{v} \cdot \Delta\vec{k}/\Delta k$. In other words, the incoherent spectrum encodes the electron velocity distribution function (EVDF) projected along the scattering vector v_k direction, which in this experiment was oriented along the azimuthal direction.

Based on this scattering model, we convert the measured wavelength, λ, to electron velocity via the resulting relation

$$v_k = \frac{c\,(\lambda_0/\lambda - 1)}{2\sin(\theta/2)}, \tag{16}$$

where c is the speed of light and λ_0 is the incident laser wavelength in the lab frame. We then fit the remaining wings of the distribution with a convolved Maxwellian model, according to the following fitting function:

$$f(\lambda_j) = H n_e r_e^2 \sum_k \frac{1}{v_T\sqrt{\pi}} \exp\left[-(v(\lambda_k) - u_d)^2/v_T^2\right] I_{j-k} \Delta v. \tag{17}$$

The quantity I_j represents the discrete point-spread function of the spectrometer: the observed spectrum is the convolution of this function with the true post-filtering spectrum. We characterized I_j experimentally by measuring and normalizing the spectrum of unfiltered stray laser light. Since the laser line-width is far narrower than a single pixel wavelength bin, the stray light is effectively a delta distribution for wavelengths, which allows this approximation. The factors H, n_e, and r_e represent a calibration factor, the electron density, and the classical electron radius (a fundamental constant), respectively; these determine the total area under the curve of the spectrum. The value of H, which encapsulates geometric factors as well as optical transmission efficiency, can be calibrated from another well-understood stimulated scattering process. We follow several other works[33,36,37] in using rotational Raman scattering from diatomic nitrogen at a known temperature for this purpose. Given these known quantities, the expression in Eq. 17 has 3 parameters:

the electron density n_e, the mean drift velocity along the scattering vector u_d, and the thermal velocity $v_T = \sqrt{2k_BT_e/m_e}$, where T_e is the electron temperature, k_B is Boltzmann's constant, and m_e is the electron mass.

Figure 4 shows several examples of Thomson spectra, with the wavelength axis converted to velocity via Eq. 16. The central regions of the spectra are not representative of the EVDF, because the value of the spectra there are distorted by laser light and attenuation by the notch filters. In some cases, the result is still a smooth curve in the central region, which is a result of convolutional broadening due to finite spatial resolution of the detector, but in other spectra a clear dip in the center of the spectrum due to this filtering is observable (for example subfigures (d) and (e)). Regardless, we reject points in the center of the spectrum from analysis and fitting, as denoted by the shaded regions in Fig. 4. We selected rejection bounds based on the width of the convolution of the filter bandwidth with the instrument function, which defines the region which can be distorted by these two effects. We generated the shown fits of Eq. 17 to the spectra with uncertainty using a Bayesian Monte-Carlo model, which is described in further detail in Appendix A. This is an algorithm for generating N probabilistic samples of possible parameter sets given random Gaussian noise in the measurement, which are then used to propagate uncertainty to further calculations based on these fluid parameters.

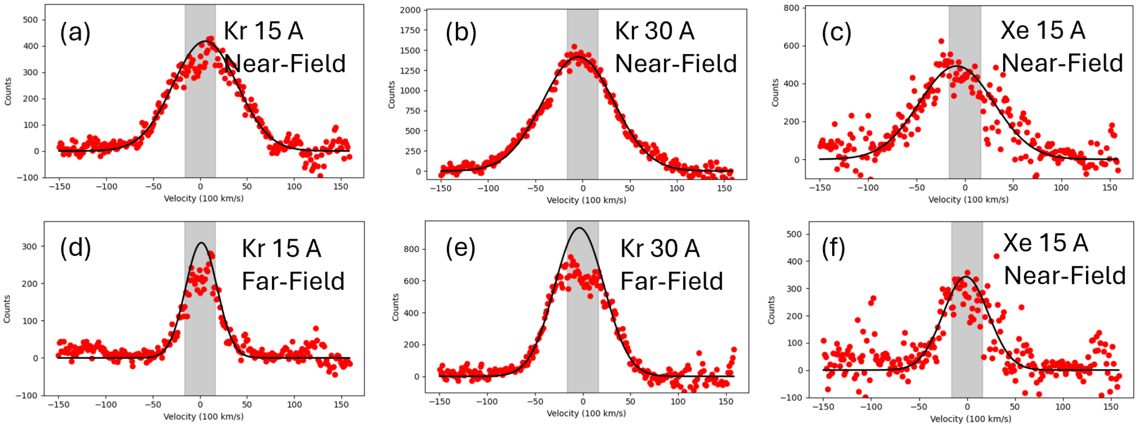

Figure 4. Examples of azimuthal EVDFs with Maxwellian fits in the Hall thruster plume. The shaded region corresponds to the notch filter bandwidth, and is excluded from the fitting.

C. Laser-Induced Fluorescence

While the ITS diagnostic provides measurements of the electron velocity distribution, which can be reduced to effective values for the electron density, velocity, and temperature within the limit that the distribution is near equilibrium, this is not sufficient to characterize the electron transport properties of interest in the plasma. This is because the slow diffusion of electrons across field lines is comparable to the ion velocity by current conservation. The electron velocity (in the cross-field direction) is thus far smaller than the electron thermal speed, and accordingly falls far below the bulk drift detection limit for the Thomson diagnostic. However, the electric field and ion dynamics can be resolved with laser-induced fluorescence velocimetry, which assists in this regard.

For this work, we leverage LIF measurements previously reported in Ref. 38. In that work, a dual-laser LIF velocimetry system was constructed to measure the velocities of both singly-ionized xenon and krypton in the H9 at the same operating conditions in Tab. 1, which we describe briefly in the following. The system is comprised of two tunable diode lasers, which are tuned to excite a metastable xenon ion state at a vacuum wavelength of 834.953 nm,[39] and a similar state in the krypton ion at a wavelength of 729.18 nm. When ions interact with these photons and are excited to a higher state, they subsequently decay, emitting a characteristic fluorescence in the visible electromagnetic band. For an ion at rest, the natural linewidth of this transition is relatively narrow — However, moving ions will only be excited by a Doppler-shifted wavelength. Since this fact provides a means of mapping wavelength to ion velocity, tuning the laser and monitoring the intensity of fluorescence provides a means to approximate the ion velocity distribution function (IVDF) along the laser axis.

A dichroic mirror combines these two beams into the same optical path, where they are sampled for power and wavelength measurement before passing through a mechanical-optical chopper. The chopper modulates the beam power at a known frequency in the neighborhoods of 1-3 kHz to facilitate phase-sensitive detection (PSD) and improve signal-to-noise. Following chopping, the diode beams are focused into a 50-um optical fiber, which passes the light through a feedthrough into the vacuum chamber. Within the chamber, a 50-mm-diameter lens focuses the fiber output to a spot within the thruster plume. A similar collection optic to the ITS system collects fluorescence from the plasma at an oblique angle. The fluorescence process relies on spontaneous, uniform emission of photons at all angles, so the collection optic direction does not affect the spectrum. This collected light is then fiber-coupled to a photomultiplier tube (PMT), before analog PSD and digitization performed by a lock-in amplifier (SRS 830) unit.

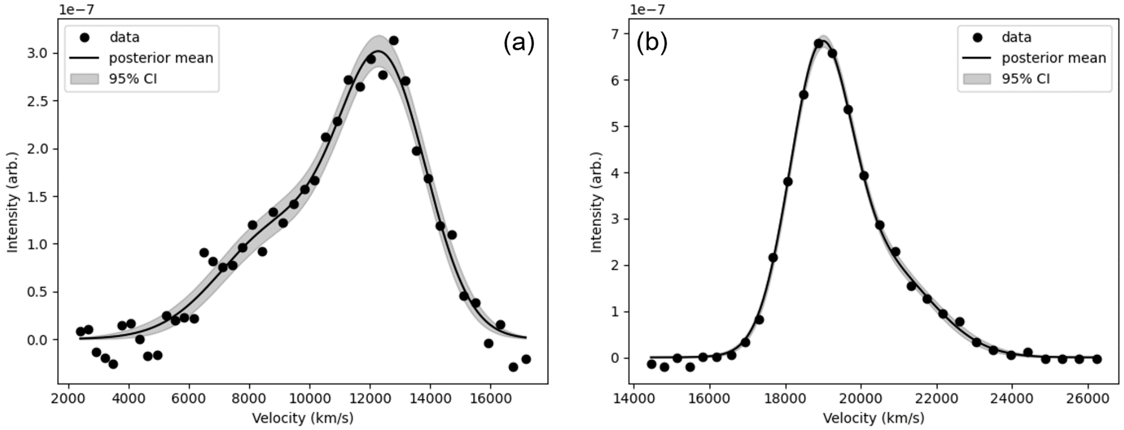

Figure 5. Example axial LIF traces, with most likely fits and 95% credible intervals for the fit based on a Bayesian noise model. (a) mid-acceleration region. (b) downstream edge of domain.

Like the Thomson scattering diagnostic, the working principle of the LIF diagnostic is based on the Doppler shift of the laser photons between the lab frame and the moving ions. However, rather than measuring the passive Doppler shift of the scattered light, LIF instead uses a tunable laser to selectively excite ions moving at different velocity projections along the incident laser wavevector, $\vec{k}_{i,LIF}$. Thus, when the laser is tuned to a wavelength λ, excitation and fluorescence occurs in ions which are moving at a velocity such that in their reference frame, the incoming photons are shifted to the transition center wavelength, λ_0. This leads to the wavelength/velocity conversion

$$v_{LIF}(\lambda) = c(\lambda/\lambda_0 - 1). \tag{18}$$

In a similar way to ITS, then, the LIF spectra can thus be converted to (unnormalized) probability distributions over ion velocity.

Example LIF spectra are shown in Fig. 5. Our injection optic was oriented in order to measure axial velocity projections, as illustrated in Fig. 1. Since the spectra are generally non-equilibrium due to the low collision rate in the plume as well as averaging over the breathing mode oscillations, we adopt a double-Gaussian fitting function to capture large tails and other asymmetric features:

$$f_i(v|c_i) = c_1 \exp\left[-(v-c_2)^2/c_3^2\right] + c_4 \exp\left[-(v-c_5)^2/c_6^2\right]. \tag{19}$$

We used the same Bayesian scheme as for the ITS data for generating probabilistic samples of likely fits to the curves with a Markov-Chain Monte Carlo algorithm (see Appendix A). To compute the ion velocity and electric field, we used the moment method of Pérez-Luna et al.[40] to integrate each sample for the IVDF fit and generate a corresponding sample of the axial components of the velocity and electric field.

For both diagnostics, we obtained spatial resolution by translating the thruster on a 3-axis motion stage. We periodically realigned injection optics with motorized stages within the chamber. For Thomson scattering, the cathode was used as an alignment reference, and the injected laser was aligned to maximize the scattering signal from this location. Meanwhile, to realign the LIF apparatus, we coupled visible diode lasers through the injection fibers and aligned the optics relative to a painted spot of boron nitride paste on the front corner of the outer pole.

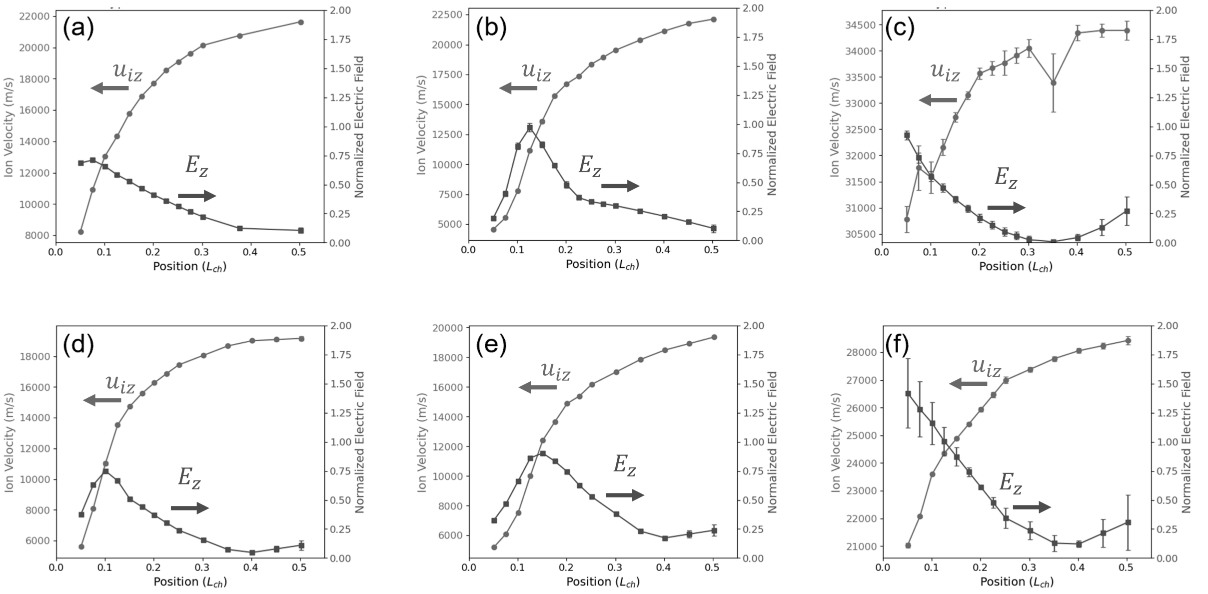

Figure 6. Axial velocity of singly-charged ions and electric field inferred from laser-induced fluorescence data. (a) Krypton, 300 V, 15 A. (b) Krypton, 300 V, 30 A. (c) Krypton, 600 V, 15 A. (d) Xenon, 300 V, 15 A. (e) Xenon, 300 V, 30 A. (f) Xenon, 600 V, 15 A.

IV. Results

In this section, we examine the plasma properties observed with the combined ITS and LIF investigations and note their dependence on propellant, discharge current, and discharge voltage. We then compute the effective inverse Hall parameter, which quantifies the local cross-field electron transport, as a function of propellant and operating condition. Finally, we present the results of a 2D mapping of the thruster plume with the goal of assessing isothermality along magnetic field lines.

A. Centerline Ion Properties

Figure 6 shows the results of laser-induced fluorescence ion velocity data for the operating conditions in Table 1 (other than the 400-V operating condition, which is not shown). Displayed in blue are the mean ion velocities obtained from computing the first velocity moment of the fit to the IVDF, while the red curve corresponds to the normalized electric field profile. We inferred the electric field using the Pérez-Luna method based on the first three moments of the distribution.[40] This method depends on the derivatives of the moments of the distribution; we estimate these derivatives by fitting a smoothing spline to the moments as a function of position, and analytically differentiating. We capture uncertainty in this derivative by repeating this process for each set of 2000 samples of the ion curve fits (see Appendix A.).

These ion velocity and electric field data are then interpolated onto the slightly different set of locations outside of the thruster channel for which we have Thomson scattering measurements. These LIF results, which were first presented in Ref. 38, are similar for xenon and krypton, except for the fact that krypton reaches higher final speeds due to its low mass. As noted in that work, there is an axial shift in the electric field and ion velocity profile which results from changing the thruster operating condition. Relative to the 300-V, 15-A case, for which the electric field peak is located just beyond the channel exit (Fig. 6(a)), increasing the discharge current to 30 A results in a downstream shift in the peak electric field from 0.1 to

0.15 channel lengths for both xenon and krypton. Likewise, when the discharge voltage is increased to 600 V, the electric field shifts in the opposite direction, such that the peak is located within the channel. When combined with knowledge of the electron heating and expansion in the plume, these electric field profiles can be directly used to estimate the mobility of electrons across field lines in the thruster.

B. Centerline Electron Properties

Figure 7 displays the electron fluid parameter results from the fits to the Thomson scattering spectra at several operating conditions. In Fig. 7(a), we display the effective azimuthal electron temperature on channel centerline for four combinations of discharge current and voltage (c.f. Tab. 1). We see from these results that for operation on krypton, the electron temperature generally decreases with distance from the thruster. This is expected, as we anticipate a region of Ohmic heating due to the increased electron resistivity where the magnetic field is maximized, near the thruster exit plane ($z = 0$). For all operating conditions, the peak values for electron temperature fall between 65 and 120 eV. However, the temperature appears to continue to increase within the channel, where we lack optical access. Relative to the 300-V, 15-A operating condition, the peak temperature outside of the channel increases slightly with increased current, and moreso with increased discharge voltage. This is roughly consistent with the traditional scaling law in Hall thrusters, which states that the electron temperature should scale proportionately with the applied voltage. However, despite having the same proportionality, we note that the precise values actually exceed that predicted by the scaling law of $T_e \approx 0.1V_D$ in unshielded Hall thrusters.[41] These values are, however, consistent with previous Thomson scattering measurements of the acceleration region in magnetically shielded Hall thrusters, which have all demonstrated $T_e > 0.2V_D$.[15,16]

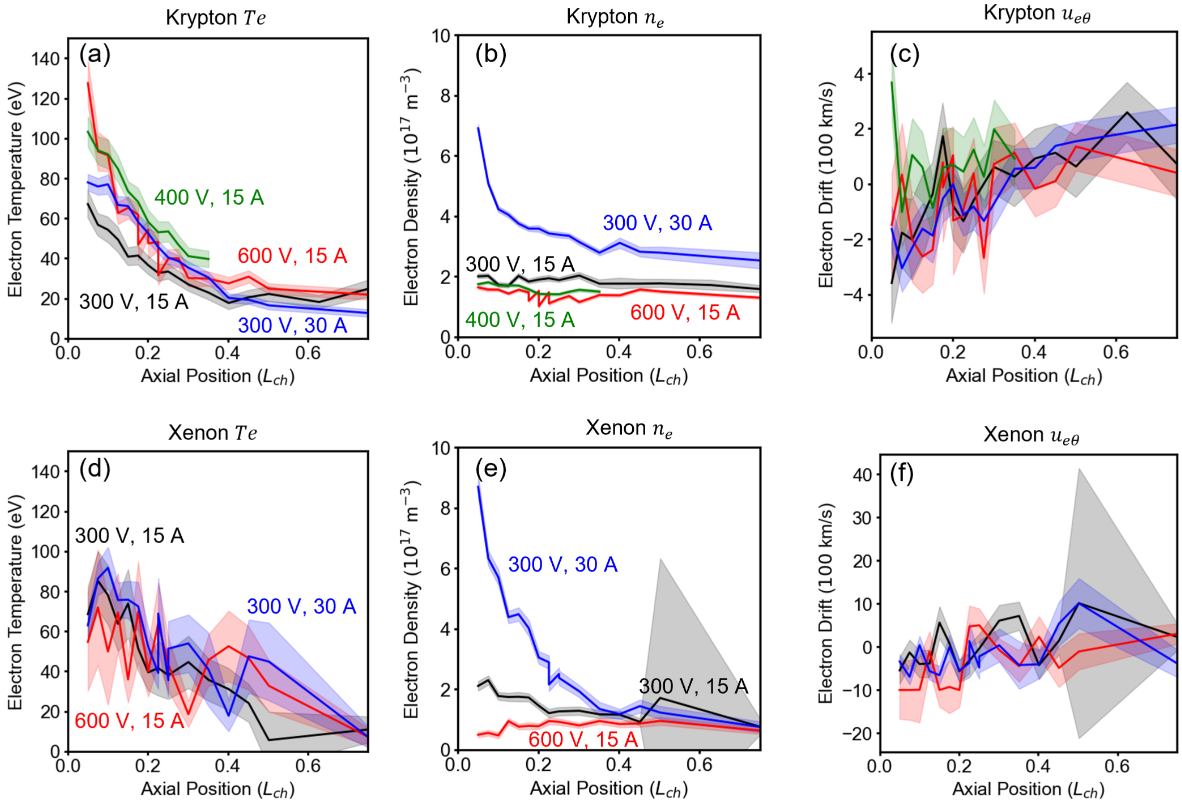

Figure 7. Electron fluid parameters extracted from ITS measurements on channel centerline. (a) Electron temperature (krypton). (b) Electron density (krypton). (c) Azimuthal electron drift (krypton). (d) Electron temperature (xenon). (e) Electron density (xenon). (f) Azimuthal electron drift (xenon).

Figure 7(d) shows the electron temperature results for the thruster operating on xenon propellant at similar operating conditions. The uncertainty values stemming from the Maxwellian fits to the azimuthal

EVDFs are larger for the xenon data, due to the increased noise arising from stronger plasma radiation. Despite the increased variance, the xenon temperature profiles are qualitatively similar to those for krypton operation, with peak temperatures ranging from 70 to 95 eV. For both the 300V, 15A and 300V, 30A operating conditions, a modest maximum is visible in the electron temperature, suggesting that the acceleration region lies just outside of the channel for these cases. For the 600-V case, temperatures decrease - however, it is likely that the peak temperatures are located within the channel and outside of the interrogation domain for this case. Also, this decrease is not statistically significant given the larger credible intervals at 600 V. For both gases, the electron temperature generally decays to below 20 eV far from the thruster. These results not only repeat the previous finding of large electron temperatures in magnetically shielded thrusters,[15,16] but also confirm that similarly large temperatures are present for operation on xenon propellant, and appear to scale with the expected proportionality with discharge voltage and current. Upon comparison with Fig. 6, we find that the peak in electron temperature occurs slightly upstream of the peak in electric field.

Figures 7(b) and (e) display the electron density variation in the near-field plume. For both krypton and xenon, the 300-V, 15-A density values both generally decrease from $2 \cdot 10^{17}$ to $1 \cdot 10^{17}$ m^{-3} with distance away from the thruster. For the 400-V and 600-V traces, the densities are slightly lower and noisier, but no variation greater than a factor of two occurs. However, in the 30-A case, in which we would expect a downstream shift in the ionization and acceleration region downstream based on the electric field profile (c.f. Fig. 6), we observe an increase in the peak densities for both propellants, both ranging from $\sim 8 \cdot 10^{17}$ to $\sim 1 \cdot 10^{17}$ within the domain. Presumably, we are observing the downstream section of the ionization region in this case. This density scaling behavior further corroborates the results inferred from the electron temperature profiles, namely that the electron properties shift axially with discharge voltage and current in the same manner as the electric field.

Finally, Figs. 7(c) and (f) display the drift velocities in the azimuthal direction inferred from the EVDF fits. Due to the noise in the measurement at certain operating conditions, especially those with higher voltage, the inferred drift has varies by several hundred km/s across the domain. However, we here point out several notable features of these results, which particularly apply to the higher-confidence EVDF fits at 300V, 15A and 300V, 30 A for krypton. The electron drift is in the negative direction in all cases and generally decreases in magnitude with distance from the thruster. This is consistent with the fact that for this study, the thruster magnetic field coils were operated with the opposite polarity as in a previous study, when we measured drifts in the positive direction.[16] We also observe peak drift speeds on the order of 300 km/s, whereas during the previous study we observed a peak of higher drifts of up to 800 km/s before a decrease to similar values on the order of 300-400 km/s. This minor discrepancy could be due to a small difference in alignment, based on the fact that the peak velocity is located at the edge of or inside the channel. Alternatively, the previous measurement was obtained with half the spectrometer slit width (500 µm vs. 1000 µm), leading to a factor of two narrower instrument broadening function, and in turn superior velocity resolution.

C. Effective Collision Frequency

For each operating condition, we can estimate the total inverse Hall parameter, Ω^{-1}, by combining the plasma parameters inferred from the LIF and ITS results (c.f. Sec. IIA). The inverse Hall parameter is a normalized quantity that directly reflects the enhanced total electron collision frequency required to balance the electron momentum in the axial direction. For our purposes, we ignore the relatively small contribution of the classical collision frequency and equate the total collision frequency to the anomalous collision frequency, i.e. $\nu_{AN} \approx \nu_{tot}$. This is a good assumption in the near-field plume, where the magnetic field is large; however, deeper into the channel, classical collisions can dominate.[42] We show the results of these computations in Fig. 8, with 95% credible intervals propagated from the Bayesian fitting uncertainties. The order of magnitude of the inverse Hall parameter ranges in all cases between 10^{-3} and 1. This is generally consistent with previous estimates of this quantity based on analytical and numerical models which were calibrated by probe mesaurements and LIF studies.[9,42,43] In some cases, the uncertainty in our measurements is large enough that the argument of the square root in Eq. 3 becomes negative. This mathematically corresponds to the calculated azimuthal drift being lower than can be explained by a finite collision rate, given the computed axial drift. We therefore omit these unphysical points by requiring that the computed azimuthal drift velocity remain semipositive-definite.

For krypton, the inverse Hall parameter (shown in Fig. 8(a)) for the baseline operating condition of 300 V, 15 A gradually increases with distance from the thruster from below 10^{-2} to $3 \cdot 10^{-2}$. This is qualitatively in line with our results from a previous study at the same operating condition, in Ref. 16. In this work, we have corrected for the contribution from multiply-charged ions, which affects our estimate of the total current carried by the plasma, resulting in small changes in the absolute value of the collision frequency. Increasing the discharge current to 30 A exposes a local minimum in the anomalous collision frequency profile near 0.1 channel lengths from the exit plane. This is consistent with the downstream shift in the electric field peak and temperature profile found in Figs. 6 and 7. For the operating conditions with increased discharge voltage and krypton propellant, the inverse Hall parameter rises in magnitude to above 0.1 over the majority of the domain. We note that the discharge current oscillations were severe, reaching 100% peak-to-peak, for these cases. However, these higher values could be due to the dip in the inverse Hall parameter shifting upstream, commensurate with the behavior of the electric field and temperature profiles at higher voltages.

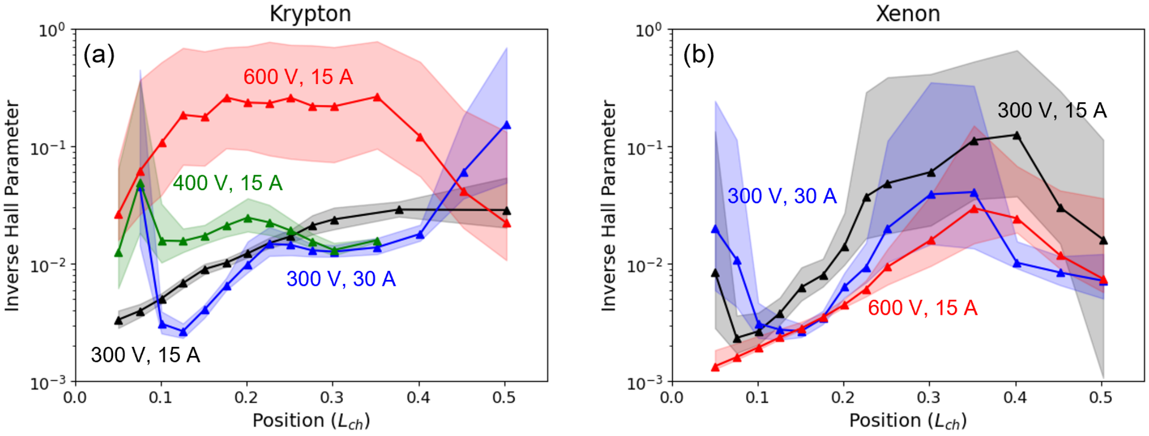

Figure 8. Comparison of the inverse Hall parameter, estimated from combined ITS and LIF measurements at different operating conditions and propellants. (a) Krypton. (b) Xenon.

Turning to the estimation of the inverse Hall parameter for the H9 operating with xenon propellant (Fig. 8(b)), we find that a local minimum is observable in both the 300 V, 15 A and 300 V, 30 A cases. Further, we observe a distinct downstream shift by approximately 0.05 channel lengths in the location of this local minimum, which is again consistent with the movement of the electric field and electron temperature profiles. For 600-V operation on xenon, the inverse Hall parameter increases gradually through the plume, but the local minimum is not accessible if present further upstream. For xenon, all three of the profiles reach a downstream maximum before reducing slightly. While it is possible that this is a real effect, it also may be due to the sensitivity of the calculation to very small azimuthal drift velocities in this region, resulting from the reduced electric field and temperature gradient. Ultimately, better knowledge of the axial electron drift speed and effects of thruster divergence are necessary to confirm this behavior. It is interesting to note that while the 300 V, 15 A and 300 V, 30 A conditions have qualitatively similar behavior for the two propellants, the behavior at 600 V, 15 A is significantly different. One explanation is that the large discharge current oscillations which are present for krypton at 600 V, which are not present when operating on xenon, alter the anomalous transport dynamics in some way. Alternatively, the acceleration region may have shifted further into the channel for this case, so that we are observing the downstream transport properties. Other than at the highly oscillatory conditions of 400 V and 600 V operation on krypton, however, we note that across both propellants, the anomalous transport profiles are remarkably similar qualitatively and in absolute range.

D. 2D Electron Property Maps

The results of our operating condition study in the previous section show that for all operating conditions and propellants tested, the peak effective azimuthal electron temperatures are quite large, ranging from 65 to above 100 eV. Previous fluid models, in which the anomalous collision frequency was calibrated based on LIF data alone, generally predict lower peak temperatures for these operating conditions by a factor of ~ 2.[18,42] For the energy equation, these models assume a Fourier-law heat flux based on this anomalous collision frequency, but did not directly calibrate the electron energy equation (See Sec. II.B). A particular feature

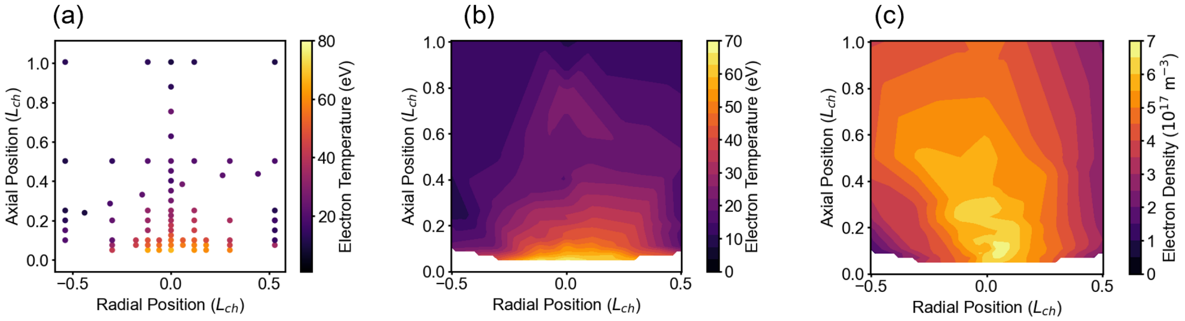

Figure 9. Axial-Radial ITS maps of the azimuthal electron properties for the H9 operating at 300 V, 15 A. (a) Scatter plot of measurements with color corresponding to the electron temperature. (b) Interpolated electron temperature contours. (c) Interpolated electron density contours.

of these models is that along field lines, electron heat flux is assumed to scale based on the low, classical collision rate; this results in a very large parallel heat flux compared to perpendicular, and in turn in nearly isothermal field lines. This surprising finding that the electron temperature is so large in the acceleration region warrants a reconsideration of the energy transport mechanisms in the thruster plume, both across and along magnetic field lines. To accomplish this, we investigated the variation of the electron properties in a 2D, axial-radial plane in front of the H9 channel at the baseline operating condition of 4.5 kW (300 V, 15 A) on krypton propellant.

In Figure 9, we display the results of a sparse 2D sweep of the azimuthal EVDF properties in the axial-radial plane. Figure. 9(a) shows the scatter plot of points in r-z space, where the color corresponds to the electron temperature. We then interpolate linearly between these measurements to generate electron temperature contours, shown in Fig. 9(b). Figure 9(c) displays the plasma density contours within the same domain. It is evident that instead of the temperature contours following the magnetic field lines, the relatively hot, dense region of the plasma is confined to the center of the channel. The electrons cool from above 60 eV to below 10-15 eV at both the inner and outer edge of the channel. This is strikingly different from the widely held assumption that the field lines are nearly isothermal as a result of high parallel heat transport relative to perpendicular heat transport. For the electron temperature to vary so strongly along field lines, the transport of heat by electrons must be much lower than expected in the parallel-field direction. In Section V.B., we discuss possible mechanisms for this heat trapping.

V. Discussion

In this section, we first examine trends in the estimated inverse Hall parameter with respect to local plasma properties in order to assess the scaling of anomalous momentum transport. We then propose a closure model for the inverse Hall parameter based on the scaling of the effective collision frequency with the azimuthal electron Mach number. Following this, we discuss mechanisms for the reduced heat flux along magnetic field lines which is needed to explain the large electron temperatures and variation along magnetic streamlines which we observed in the previous section.

A. Empirical Scaling of Anomalous Collisions with Plasma Properties

Due to the non-classical nature of the electron momentum transport across magnetic field lines in Hall thrusters, the standard model equations for conservation of momentum and energy of each plasma species is left open; that is, the values of Ω^{-1} and $\vec{q}$ throughout the plasma must be predicted in order to develop a predictive model. While recent work strongly suggests that the first-principles mechanism for producing these enhanced effective "collisions" arises from nonlinear interactions with plasma turbulence,[6,44,45] it is not yet clear how, if at all, the macroscopically averaged forces from the these wave interactions depends on the plasma properties in a manner which could be predicted self-consistently by a fluid model of the electrons.

Given this motivation and the new, direct transport information provided by the combined LIF-ITS diagnostic, it is therefore critical to investigate the scaling of the inferred anomalous transport profiles with the background plasma properties. For example, Lafleur et al. suggest that the anomalous collision frequency may scale with the plasma density.[46] We note also, that as pointed out by Simmonds et al.,[13] the scaling of ν_{AN} with n_e has a large effect on the theoretical upper limit of Hall thruster performance. In Fig. 10(a), we aggregate our evaluations of the inverse Hall parameter at all positions and operating conditions in order to quantify the density dependence. We note that there is no strong trend given the variance of the data. This is consistent with the fact that global performance measurements of Hall thrusters operating at high current densities have shown only a slight change in electron current fraction across the field lines.[14] However, within a particular operating condition dataset, in most cases, Ω^{-1} decreases with the density. Thus, it is possible that a composite scaling law accounting for other parameters, for example the magnetic field strength, could describe the data.

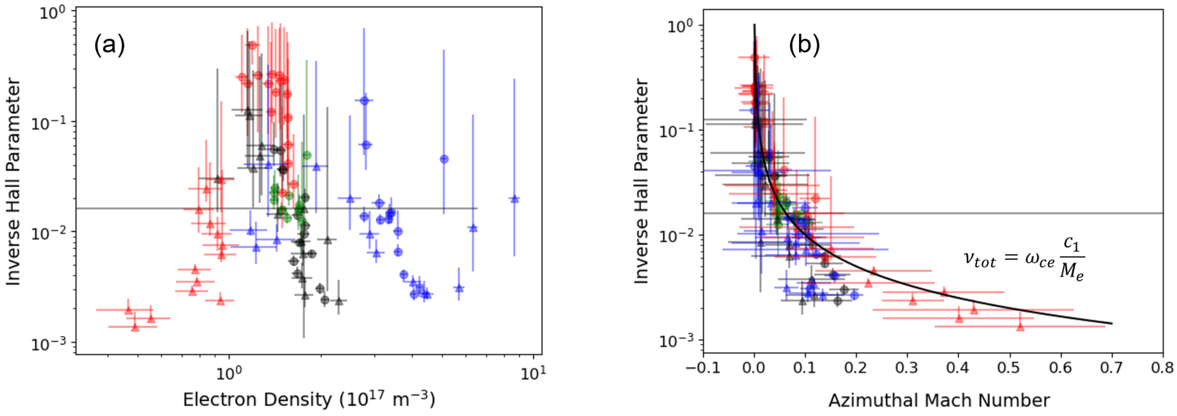

Figure 10. Scaling of the anomalous collision frequency on all propellants and operating conditions with plasma properties. Krypton data is represented by circles, while xenon data is represented by triangles. (a) Inverse Hall parameter vs. density. (b) Inverse Hall parameter vs. electron Mach number, with our empirical scaling law. The tuning parameter c_1 is chosen to be 0.001.

Another parameter which we might expect to play a role in the anomalous momentum transport is the electron Mach number, $M_e = u_{e\theta}/v_{Te}$, in the azimuthal direction (where $v_{Te} = \sqrt{2k_B T_e/m_e}$). Since the azimuthal electron drift is the energy source for instability modes which grow unstable in the plume,[6,47] the local value of this drift may contain information about the wave amplitudes and the nonlinear forces which are transferred to the electrons, potentially inducing anomalous transport. In Fig. 10(b) we show the scaling of the inverse Hall parameter with the azimuthal electron Mach number. Due to the noise in our direct measurements of of the azimuthal ion velocity, we instead estimate the azimuthal drift in this case based on the electric field and measured temperature gradient, which we know from these measurements with greater certainty. We previously validated that the actual electron velocity does agree well with the computed drift speed in this thruster when performing an experiment with higher spectral resolution but lower light throughput.[16] Provided that the electrons are strongly magnetized ($\Omega^{-1} < 1$), this is a good approximation.

In contrast to the density, there is a clear correlation between the inverse Hall parameter and the electron Mach number. For both xenon and krypton, the anomalous collision rate as a function of electron Mach number approximately collapses to the same curve. We approximate this scaling empirically with the formula

$$\nu_{tot} = \omega_{ce}\frac{c_1}{M_e}, \tag{20}$$

where c_1 is a tunable parameter. For both xenon and krypton, choosing the parameter $c_1 = 10^{-3}$ fits the data at all operating conditions and propellants remarkably well. The M_e^{-1} dependence was chosen to best fit the data, however given the uncertainty in the azimuthal Mach number, other decaying functions may be possible. We note that the black and blue points with the largest deviation, which represent the near-field properties when the thruster is operating at the lower voltage of 300 V, correspond to points for which the plasma density and neutral density are larger due to the ionization region protruding from the channel. As a result, it is possible that the deviation could be remedied by accounting for the difference between ν_{tot} and ν_{AN}, which scales with the neutral density when electron-neutral collisions dominate. Alternatively, these points could demonstrate a slight scaling with density which is not evident in Fig. 10(a).

This finding has significant implications, both practical and theoretical, for the modeling of Hall thrusters and other $E \times B$ discharges. To illustrate this, we below use rough approximations to relate the proposed scaling law to more fundamental quantities in the plasma. Based on the potential and pressure gradients which give rise to the azimuthal drift, the electron Mach number can be written as

$$M_e \approx \frac{E_z + \nabla(n_e k_B T_e)/(e n_e)}{B\sqrt{2k_B T_e/m_e}}. \tag{21}$$

Substituting this into Eq. 20 and approximating the pressure gradient as $\nabla p_e \sim p_e/L_p$ for the gradient lengthscale L_p, our closure for the (anomalous) total collision frequency can be written in terms of elementary plasma properties as

$$\nu_{tot} \approx \nu_{AN} = c_1 \frac{eB_r^2}{m_e^{3/2}} \frac{\sqrt{2k_B T_e}}{E_r + k_B T_e/(eL_p)}. \tag{22}$$

Finally, we make the simplifying approximation that the electron temperature is constant as the magnetic field strength is varied. With this scaling, we recover the scaling that for constant electron temperature,

$$\nu_{AN} \propto B^2. \tag{23}$$

This closure has the counter-intuitive implication that if the radial magnetic field strength is increased, the electron confinement is reduced, promoting increased cross-field transport. On the other hand, if T_e varies as B is changed, the scaling with magnetic field may be more or less steep. Lastly, this expression is independent of the plasma density, which is consistent with observations of minimal degradation to Hall thruster performance during tests at increased current densities,[14] and upper limit to the achievable thrust with Hall thruster technology.[13] However, testing at higher current densities is necessary to verify that this independence is preserved over a larger range of values.

B. Mechanisms for Temperature Variation Along Field Lines

In addition to closing the momentum transport law by specifying the inverse Hall parameter, it is necessary to capture non-classical effects in the electron energy balance to accurately model the Hall thruster discharge. Fluid models generally compute a thermal conductivity based on collisional effects. Classically, for a magnetized electron fluid, the thermal conductivity in the parallel-field direction is much larger than the perpendicular conductivity. This leads to the widely simulated result that magnetic field lines are isothermal. Additionally, studies with wall-mounted and injected Langmuir probes have measured similar temperatures at multiple points along magnetic field lines in the acceleration region of unshielded Hall thrusters, and upstream of the acceleration region in a magnetically shielded thruster.[17] However, this is not consistent with our Thomson scattering results from the H9 thruster plume. Based on Fig. 9, the electrons are far hotter on channel centerline than at the channel edge, ranging from > 60 eV to < 20 eV in the parallel-field direction. It is therefore necessary to discuss the nature of electron heat transport in this plasma environment to motivate an explanation for the anisothermal field lines.

To visualize the energy flow along magnetic field lines, we plot in Fig. 11 the electron temperature over density on a dual logarithmic scale, interpolated linearly along four magnetic field lines in the near-field plume. This allows us to invoke a polytropic description of the field-aligned heat flow (c.f. Eq. 14), in order to gain intuition for the electron heating and cooling mechanisms. Figure 11(a) shows the data on the left hand side of Fig. 9, which lies on the cathode/inner pole side of the channel while Fig. 11(b) displays data from the right hand side (outer pole) of the channel center line. On both plots, we display a dashed line with a slope commensurate with the three-dimensional adiabatic expansion of the electron fluid for reference. For both sides of the channel center line, the electrons along each field line scale nearly adiabatically in the region of hottest temperatures, corresponding to the center of the channel. This is the limit in which there is no internal heat flux, i.e. the electron fluid exchanges no energy with its environment as it expands.

Meanwhile, on the left (inner pole) side, the electron temperatures plateau as the density continues to fall, leading to isothermal ($\gamma \sim 1$) behavior along the field line in that region. This inner-pole behavior

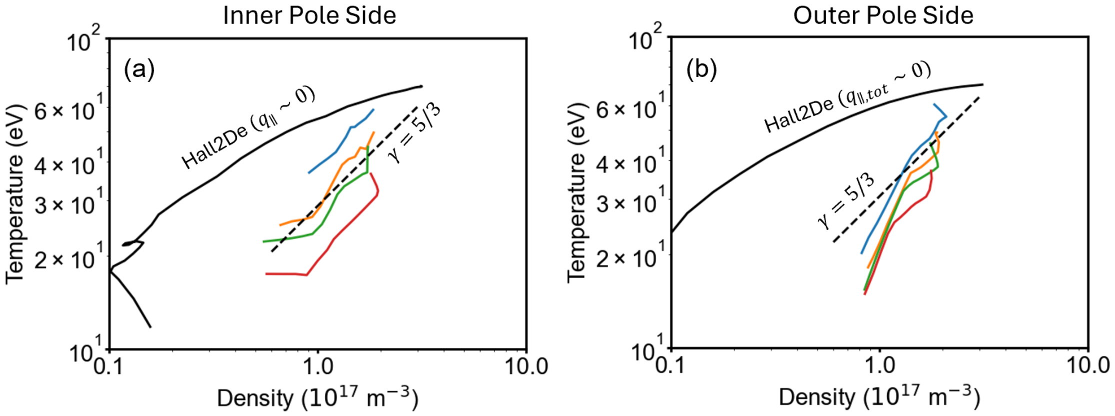

Figure 11. Logarithmic scaling of electron temperature with plasma density, along four magnetic field lines in the H9 near-field plume for operation at 300 V, 15 A on krypton. The dashed line shows the slope corresponding to adiabatic expansion ($\gamma = 5/3$), while the solid black line shows a simulation result with classical parallel heat flux reduced by a factor of 10^6. (a) Inner pole (cathode) side of plume. (b) Outer pole side of plume.

represents the opposite limit to adiabaticity, in which the parallel heat flux, $q_{\parallel}$, is sufficiently large that the electrons reach thermal equilibrium with their surroundings faster than they convect and expand.[29] On the outer pole (right) side of the channel, we observe the opposite behavior. The inflection after the adiabatic region is to an even higher slope close to $\gamma = 3$, or superadiabatic behavior.[48] The temperature falling faster than adiabatic scaling in this way can potentially be explained in a few ways. Firstly, it is possible that the electrons effectively transport energy across magnetic field lines in this region, leading to increased cooling. Another possibility is that the collisionality decreases to the point that the parallel-field temperature cannot equilibrate with the perpendicular electron temperature. In this regime, the effective thermodynamic degrees of freedom could decrease from 3 to 1 or 2 as the electrons expand, leading to larger adiabatic limits of 2 or 3, respectively, as has been demonstrated a magnetic nozzle plasma.[49] Finally, this expansion framework may not be a good model at all for the variation of the electron plasma properties along field lines far from the channel center. For example, if magnetic mirroring or some other effect which spatially confines the electrons is dominant, the sharp decrease in temperature may be due to a boundary between different electron populations altogether.

This variation in electron temperature along field lines, which transition from adiabatic expansion behavior to isothermality and superadiabaticity on either side of the channel, implies that modifications must be made to the heat flux term in fluid models for the electron population. To this end, we also display in Fig. 11 the results of a preliminary simulation using the fluid code Hall2De[25] for the H9 which used the collision frequency inferred from the ITS data, but the energy equation was modified. The plots show a field line further upstream compared to the experimental measurements. Instead of using the cross-field non-classical collision frequency to estimate a heat flux with collisional scaling (c.f. Sec. II.B), this simulation assumed only classical cross-field heat flux and set the heat flux parallel to field lines to the classical scaling, but reduced by a factor of 10^6. We see that with this imposed heat trapping, the simulation is able to reach the large observed temperatures, and correctly the qualitative nature of the temperature variation along field lines - the field line is close to isothermal in the center of the channel, but the slope steepens toward adiabatic as the electrons expand to lower densities. However, even this reduced-parallel-heat-flux model does not capture the immediate steepness of the measured temperature gradients in the center of the plasma. In any case, the mechanism for this reduced heat flux in the parallel direction must be found. We note that in a companion paper,[20] other mechanisms for accounting for the energy transport in fluid models are investigated without modifying the parallel heat flux assumptions.

One way of explaining why fluid models overestimate the heat flux density along field lines is to point to the low classical collisionality in the discharge, which invalidates classical fluid formulations for heat transport. To motivate this, we note the Knudsen number, $\mathrm{Kn} = \lambda_{mfp}/L_{\nabla p}$, for the electrons along field lines, where λ_{mfp} is the mean free path for electron-electron collisions, and $L_{\nabla p}$ is the pressure gradient length scale. Given the ITS measurements of the electron properties, Kn is on the order of 10000 in the near-field plume, as shown in Fig. 12(a). This large Knudsen number suggests that the electrons are highly non-collisional, at least ignoring the non-classical effects of plasma turbulence. In this effectively collisionless limit, the Spitzer-Harm/Braginskii heat flux formula commonly used to justify isothermality of magnetic field lines does not apply, since the electrons are highly likely to freely stream along field lines and carry heat to the pole cover/channel walls before encountering any collisions.[24,50]

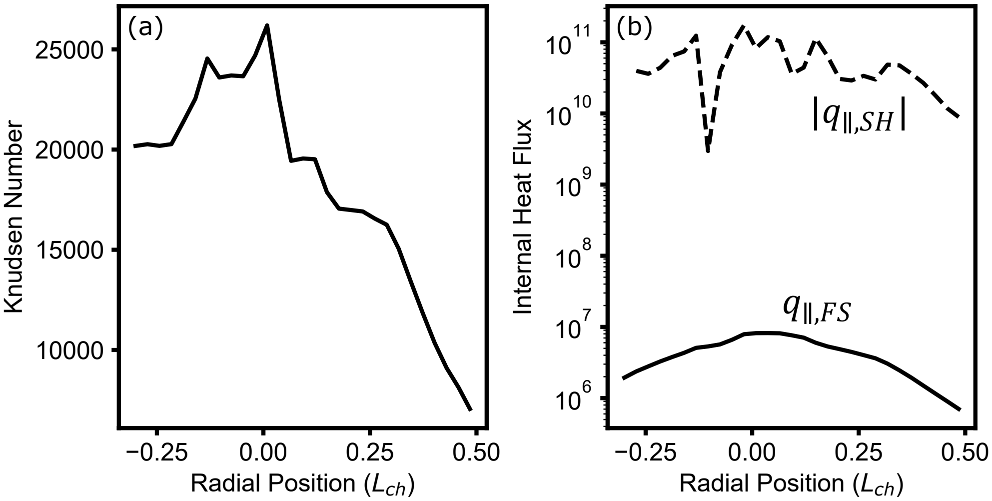

Figure 12. (a) Electron Knudsen number due to classical ion collisions along the orange field line from Fig. 11. (b) Comparison between the Spitzer-Harm heat flux density and the free-streaming limit along field lines (in units of W/m^2).

Parallel-field electron heat transport is better described in this collisionless regime by the idea of *nonlocal* heat transport, since in the absence of collisions, the flux of energy in a particular region may depend strongly on the plasma conditions far away from the immediate neighborhood. In this sense, we would not expect the heat flux $\vec{q}$ in a particular location to scale with the local temperature gradient ∇T_e, but rather be a more abstract quantity derived from the EVDF that results from electrons freely streaming through that location.[27] This situation is common in laser plasma physics, studies of the tokamak scrape-off-layer, and solar physics.[51–55] In these contexts, it is typical to compare the collisional, Spitzer-Harm/Braginskii heat flux, q_{SH}, with the free-streaming limit, $q_{FS} = n_e T_e v_{Te}$, which we display in Fig. 12(b).[50,56] This free-streaming value sets an upper limit for the rate at which energy can be convected by thermal electrons along field lines. It is clear from this comparison that the collisional formulation overpredicts the possible heat transport along magnetic field lines by approximately four orders of magnitude. Further, we note that in other plasma systems, q_{FS} is often further reduced by a tunable parameter to approximately 10% of its value to match data — thus, the Spitzer-Harm value is likely incorrect by an even larger margin.[50] We thus recommend that future modeling efforts focus on closing the electron energy equation, given this nonlocal and collisionless behavior, to accurately capture the physics in the Hall thruster discharge, both across and along field lines. While simple expressions such as assuming classical cross-field diffusion in the perpendicular direction with the free-streaming heat flux along field lines may provide a good approximation to the physics, we note that the heat flux is highly sensitive to slight deviations from Maxwellian electron distributions, since electrons in the tails of the distribution carry the majority of the heat. We also acknowledge that while preliminary investigations of the radial electron temperatures agree with our azimuthal measurements to within uncertainty, it is possible that the electron distribution is anisotropic in the axial direction, and that the effective azimuthal temperature which we measure is not representative of the fluid thermodynamics. Additionally, if the temperature and density vary over the breathing mode cycle, it is possible that the time-averaged Thomson scattering measurements are biased toward certain phases with denser and hotter electrons. Regardless, these measurements and inferences represent a new look into the local electron momentum- and heat-transfer dynamics both along and across field lines in the Hall thruster acceleration region, and combining these data-driven closures with first-principles modeling efforts must continue in order to reach a full understanding of the unknown physics at the heart of these phenomena.

VI. Conclusions

In summary, in this work we have addressed recent questions raised about anomalous momentum and heat transport in the Hall thruster acceleration region by systematically interrogating the plume of a magnetically shielded Hall thruster with non-invasive diagnostics. We applied ITS and LIF to measure the variation of electron and ion properties on channel center line as a function of operating condition and propellant, as well as performed a 2D mapping of the electron properties in the plume at a discharge power of 4.5 kW. By varying the discharge current and voltage, we found that for both krypton and xenon, electron temperatures are on the order of 20% of the discharge voltage at the peak of the acceleration region, in contrast to the expected 10% from scaling laws in unshielded thrusters. Trends in the location of the temperature profile match those expected from previous LIF studies: increasing discharge current shifts the peak temperature outside of the channel and leads to a slight increase in the peak temperature. Likewise, increasing the discharge voltage leads to an upstream shift in the opposite direction, but is accompanied by an increase in peak temperature to above 100 eV. While the Thomson scattering results with xenon are of lower confidence than the krypton results due to the more intense background light, similar peak temperatures and trends are observed between both propellants.

We then combined these electron property profiles with previously acquired LIF data to estimate the anomalous electron momentum transport coefficient throughout the plume, which we write in terms of the inverse Hall parameter. We found that the Hall parameter profiles generally increase with distance from the thruster and shift up-/downstream with the electric field and temperature profile. Notably, the estimated inverse Hall parameter scales consistently with the reciprocal of the electron Mach number for all operating conditions and propellants tested. This finding is an encouraging step toward the self-consistent closure of fluid models for the Hall thruster discharge.

Following proposing this momentum equation closure, we examine the electron energy flow in the Hall thruster plume. The r-z map of the electron temperature demonstrates that contrary to the predictions of fluid models, the magnetic field lines deviate from isothermality. Instead, the hot temperatures of $\sim$ 60-70 eV in the center of the channel fall to only 10-20 eV at the channel edge. Based on this data, we propose a potential energy equation closure based on a polytropic expansion law for electron expansion along field lines. We find qualitative agreement between a fluid model that imposes a reduced heat flux along field lines, making them approximately adiabatic, although the experimental temperatures fall off more quickly with density. Further, we demonstrate that due to the mean free paths for classical electron collisions along field lines, the classical Braginskii formulation used by most fluid models overpredicts the parallel heat flux by at least four orders of magnitude. This finding has direct implications for how heat transport is modeled in Hall thrusters and other low-temperature plasmas, and suggests that electron energy equation corrections based on nonlocal heat transport are potentially necessary to correctly capture the plume plasma physics.

Appendix A. Bayesian Fitting of Velocity Distributions under Uncertainty

Both diagnostics employed in this work (laser-induced fluorescence and incoherent Thomson scattering) use Doppler velocimetry to approximate a projection of the velocity distribution function (VDF) of for ions and electrons, respectively. These measurements are imperfect, and uncertainty in the "true" spectrum arises from both noise and limited information in the resolved spectrum (for example, from the missing filtered section of the ITS traces). Since the fluid parameters of interest, such as drift speed and effective temperature, depend on moments of these distributions, it is necessary to propagate this uncertainty to the final estimates of moment-derived parameters. To accomplish this somewhat rigorously, we resort to a Bayesian framework for computing such uncertainties based on modern Monte Carlo sampling algorithms.

To illustrate this, consider an approximate IVDF acquired with LIF, such as that shown in Fig. 5. We define a double-Gaussian fitting function (Eq. 19) to accurately capture non-equilibrium features of the ions. This model contains six parameters, $\vec{\theta}$, effectively corresponding to the height, mean, and width of both peaks. To construct a Bayesian inference framework around this fitting process, we represent our knowledge of these six parameter values as random variables. Our goal is to use the IVDF data, $\vec{d}$, to learn a multivariate probability distribution $p(\theta|d)$ describing the most likely values of these parameters. Bayes's theorem provides the means to describe this probability distribution:

$$p(\theta)|d) = \frac{p(d|\theta)p(\theta)}{p(d)}. \tag{24}$$

In the above expression, $p(\theta)$ is the prior probability distribution, representing our initial knowledge of the parameters before learning from the data. We prescribe uniform prior distributions on each parameter with hand-tuned bounds, so as to avoid prior bias while preventing overfitting and unphysical values (for example distributions with negative height/temperature). The "evidence", $p(d)$, is a normalizing constant which we do not compute in this work, since our sampling methods are self-normalizing. The quantity $p(d|\theta)$ is the likelihood of observing the data d given a particular set of parameters θ. To compute the likelihood, we assume that our measurement consists of a "true" model value $M(v, \theta)$ summed with a random variable η:

$$d(v) = M(v, \theta) + \eta, \quad \eta \sim \mathcal{N}(0, \sigma^2) \tag{25}$$

Our noise model assumes the noise η is distributed according to an unbiased normal distribution with variance σ^2. We design our model to learn the value of σ as a hyperparameter by assigning a prior exponential distribution, i.e. $\sigma \sim E(s)$. The e-folding length, s, was tuned to 5% of the maximum of the measured IVDF.

We generated empirical samples from the posterior distribution in Eq. 24 by using the No-U-Turn Sampler (NUTS), which is an efficient algorithm for Hamiltonian Monte Carlo.[57] This algorithm is available as part of the open-source python package 'numpyro'. For each velocity distribution, we used this algorithm to generate 1000 burn-in samples followed by 10,000 samples of the (in this case six) parameters. For each of these 10,000 samples, the model function is evaluated with the set of parameters to yield a single posterior prediction curve. Together, this consists of 10,000 possible fits to the VDF, distributed according to the posterior probability. For downstream calculations relying on moments of the IVDF, such as the mean ion velocity, we propagate this probabilistic uncertainty empirically, by simply computing the moments for each fit sample via numerical integration of the fit evaluated on a finer velocity grid. This results in a corresponding vector of 10,000 samples for the ion velocity, for example, from which further computations with 10,000-sample sets for other quantities can be carried out element-wise. This sampling took roughly 10 seconds per IVDF, running on a laptop, with acceptance probability ∼ 0.95. An identical process is followed for the EVDFs inferred from Thomson scattering, however with the 3-parameter convolved Gaussian model in Eq. 17. For these single-Gaussian distributions, the parameter samples directly correspond to meaningful effective fluid quantities such as the electron density, temperature, and drift, so these samples are used directly rather than take numerical moments of the distribution. All error bars in this text represent the central 95% credible intervals computed numerically from these 10000-sample sets.

Acknowledgments

This work was supported by a NASA Space Technology Graduate Research Opportunity (80NSSC20K1229), and the Air Force Office of Scientific Research Power and Propulsion Portfolio through a DURIP (FA9550-20-1-0191), as well as the Joint Advanced Propulsion Institute, a NASA Space Technology Research Institute. The authors would like to thank Dr. Vernon Chaplin, Dr. Thomas Marks and Declan Brick for helpful discussions, as well as Dr. Leanne Su and William Hurley for assistance with auxiliary diagnostics.

References

[1] Goebel, D. M., Katz, I., and Mikellides, I. G., *Fundamentals of electric propulsion*, John Wiley & Sons, 2023.

[2] Boeuf, J.-P., "Tutorial: Physics and modeling of Hall thrusters," *Journal of Applied Physics*, Vol. 121, No. 1, 2017.

[3] Dale, E., Jorns, B., and Gallimore, A., "Future directions for electric propulsion research," *Aerospace*, Vol. 7, No. 9, 2020, p. 120.

[4] Morozov, A., and Savelyev, V., "Fundamentals of stationary plasma thruster theory," *Reviews of plasma physics*, 2000, pp. 203–391.

[5] Boniface, C., Garrigues, L., Hagelaar, G., Boeuf, J., Gawron, D., and Mazouffre, S., "Anomalous cross field electron transport in a Hall effect thruster," *Applied Physics Letters*, Vol. 89, No. 16, 2006.

[6] Lafleur, T., and Chabert, P., "The role of instability-enhanced friction on 'anomalous' electron and ion transport in Hall-effect thrusters," *Plasma Sources Science and Technology*, Vol. 27, No. 1, 2017, p. 015003.

[7] Hofer, R. R., *Development and characterization of high-efficiency, high-specific impulse xenon Hall thrusters*, University of Michigan, 2004.

[8] Yan, L., Wang, P., Ouyang, H., and Kang, X., "Thermal analysis of the Hall thruster in vacuum," *Vacuum*, Vol. 108, 2014, pp. 49–55.

[9] Mikellides, I. G., and Ortega, A. L., "Challenges in the development and verification of first-principles models in Hall-effect thruster simulations that are based on anomalous resistivity and generalized Ohm's law," *Plasma Sources Science and Technology*, Vol. 28, No. 1, 2019, p. 014003.

[10] Cheng, S. Y.-M., "Modeling of Hall thruster lifetime and erosion mechanisms," Ph.D. thesis, Massachusetts Institute of Technology, 2007.

[11] Lopez Ortega, A., and Mikellides, I. G., "Investigations of pole erosion mechanisms in the 12.5 kW HERMeS Hall thruster with the Hall2De code," *2018 Joint Propulsion Conference*, 2018, p. 4647.

[12] Myrne, M. P., Roberts, P. J., and Jorns, B. A., "Coupling of Electrical and Pressure Facility Effects in Hall Effect Thruster Testing," *Proceedings of the 37th International Electric Propulsion Conference*, Electric Rocket Propulsion Soc., 2022, pp. IEPC–2022–377.

[13] Simmonds, J., Raitses, Y., and Smolyakov, A., "A theoretical thrust density limit for Hall thrusters," *Journal of Electric Propulsion*, Vol. 2, No. 1, 2023, p. 12.

[14] Su, L. L., Roberts, P. J., Gill, T. M., Hurley, W. J., Marks, T. A., Sercel, C. L., Allen, M. G., Whittaker, C. B., Viges, E., and Jorns, B. A., "High-Current Density Performance of a Magnetically Shielded Hall Thruster," *Journal of Propulsion and Power*, 2024, pp. 1–18.

[15] Vincent, B., Tsikata, S., and Mazouffre, S., "Incoherent Thomson scattering measurements of electron properties in a conventional and magnetically-shielded Hall thruster," *Plasma Sources Science and Technology*, Vol. 29, No. 3, 2020, p. 035015.

[16] Roberts, P. J., and Jorns, B. A., "Laser Measurement of Anomalous Electron Diffusion in a Crossed-Field Plasma," *Physical Review Letters*, Vol. 132, No. 13, 2024, p. 135301.

[17] Hofer, R. R., Goebel, D. M., Mikellides, I. G., and Katz, I., "Magnetic shielding of a laboratory Hall thruster. II. Experiments," *Journal of Applied Physics*, Vol. 115, No. 4, 2014.

[18] Mikellides, I. G., Katz, I., Hofer, R. R., and Goebel, D. M., "Magnetic shielding of a laboratory Hall thruster. I. Theory and validation," *Journal of Applied Physics*, Vol. 115, No. 4, 2014.

[19] Roberts, P. J., and Jorns, B., "Inferring Electron Heat Flux in a High-Power Hall Thruster with Incoherent Thomson Scattering," *AIAA SCITECH 2024 Forum*, 2024, p. 1957.

[20] Brick, D. G., Roberts, P. J., and Jorns, B. A., "Model Based Investigation of Anomalous Energy Transport in a Magnetically Shielded Hall Thruster," *Proceedings of the 38th International Electric Propulsion Conference*, Electric Rocket Propulsion Soc., 2024, pp. IEPC–2024–411.

[21] Fife, J. M., "Hybrid-PIC modeling and electrostatic probe survey of Hall thrusters," Ph.D. thesis, Massachusetts Institute of Technology, 1998.

[22] Davidson, R., and Krall, N., "Anomalous transport in high-temperature plasmas with applications to solenoidal fusion systems," *Nuclear Fusion*, Vol. 17, No. 6, 1977, p. 1313.

[23] Fitzpatrick, R., *Plasma physics: an introduction*, Crc Press, 2022.

[24] Braginskii, S. I., "Transport Processes in a Plasma," *Reviews of Plasma Physics*, Vol. 1, 1965, p. 205.

[25] Mikellides, I. G., and Katz, I., "Numerical simulations of Hall-effect plasma accelerators on a magnetic-field-aligned mesh," *Physical Review E*, Vol. 86, No. 4, 2012, p. 046703.

[26] Parra, F., Ahedo, E., Fife, J., and Martinez-Sanchez, M., "A two-dimensional hybrid model of the Hall thruster discharge," *Journal of Applied Physics*, Vol. 100, No. 2, 2006.

[27] Ahedo, E., Correyero, S., Navarro-Cavallé, J., and Merino, M., "Macroscopic and parametric study of a kinetic plasma expansion in a paraxial magnetic nozzle," *Plasma Sources Science and Technology*, Vol. 29, No. 4, 2020, p. 045017.

[28] Zhang, Y., Li, J., and Tang, X.-Z., "Electron heat flux and propagating fronts in plasma thermal quench via ambipolar transport," *Physics of Plasmas*, Vol. 30, No. 9, 2023.

[29] Bellan, P. M., *Fundamentals of plasma physics*, Cambridge university press, 2008.

[30] Hofer, R. R., Cusson, S. E., Lobbia, R. B., and Gallimore, A. D., "The H9 magnetically shielded Hall thruster," *35th International Electric Propulsion Conference*, Electric Rocket Propulsion Soc., 2017, pp. 2017–232.

[31] Viges, E. A., Jorns, B. A., Gallimore, A. D., and Sheehan, J., "University of Michigan's upgraded large vacuum test facility," *36th International Electric Propulsion Conference*, 2019, pp. 1–18.

[32] Su, L. L., Marks, T., and Jorns, B. A., "Trends in mass utilization of a magnetically shielded Hall thruster operating on Xenon and Krypton," *Plasma Sources Science and Technology*, 2024.

[33] Vincent, B., Tsikata, S., Mazouffre, S., Minea, T., and Fils, J., "A compact new incoherent Thomson scattering diagnostic for low-temperature plasma studies," *Plasma Sources Science and Technology*, Vol. 27, No. 5, 2018, p. 055002.

[34] Roberts, P. J., Brown, Z. A., and Jorns, B. A., "Non-invasive Characterization of Electron Mach Number in a Hollow Cathode with Incoherent Thomson Scattering," *AIAA SciTech 2023 Forum*, 2022.

[35] Allen, R. P. J., Madison G., and Jorns, B. A., "Direct Measurements of the Pressure Dependence of the Electron Temperature in a Magnetically Shielded Hall Thruster," *Proceedings of the 38th International Electric Propulsion Conference*, Electric Rocket Propulsion Soc., 2024, pp. IEPC–2024–821.

[36] Van de Sande, M. J., "Laser scattering on low temperature plasmas: high resolution and stray light rejection," 2002.

[37] Suazo Betancourt, J. L., Butler-Craig, N., Lopez-Uricoechea, J., Bak, J., Lee, D., Steinberg, A. M., and Walker, M. L., "Thomson scattering measurements in the krypton plume of a lanthanum hexaboride hollow cathode in a large vacuum test facility," *Journal of Applied Physics*, Vol. 135, No. 8, 2024.

[38] Su, L. L., Marks, T. A., and Jorns, B., "Investigation into the efficiency gap between krypton and xenon operation on a magnetically shielded Hall thruster," *International Electric Propulsion Conference, Massachusetts Institute o f Technology, Cambridge, MA, USA*, 2022.

[39] Huang, W., Drenkow, B., and Gallimore, A., "Laser-induced fluorescence of singly-charged xenon inside a 6-kW Hall thruster," *45th AIAA/ASME/SAE/ASEE Joint Propulsion Conference & Exhibit*, 2009, p. 5355.

[40] Pérez-Luna, J., Hagelaar, G., Garrigues, L., and Boeuf, J.-P., "Method to obtain the electric field and the ionization frequency from laser induced fluorescence measurements," *Plasma Sources Science and Technology*, Vol. 18, No. 3, 2009, p. 034008.

[41] Dannenmayer, K., and Mazouffre, S., "Elementary scaling relations for Hall effect thrusters," *Journal of Propulsion and Power*, Vol. 27, No. 1, 2011, pp. 236–245.

[42] Marks, T. A., and Jorns, B. A., "Challenges with the self-consistent implementation of closure models for anomalous electron transport in fluid simulations of Hall thrusters," *Plasma Sources Science and Technology*, Vol. 32, No. 4, 2023, p. 045016.

[43] Dale, E. T., and Jorns, B. A., "Non-invasive time-resolved measurements of anomalous collision frequency in a Hall thruster," *Physics of Plasmas*, Vol. 26, No. 1, 2019.

[44] Tsikata, S., Lemoine, N., Pisarev, V., and Grésillon, D., "Dispersion relations of electron density fluctuations in a Hall thruster plasma, observed by collective light scattering," *Physics of Plasmas*, Vol. 16, No. 3, 2009.

[45] Brown, Z. A., and Jorns, B. A., "Anomalous cross-field transport in a Hall thruster inferred from direct measurement of instability growth rates," *Physical Review E*, Vol. 108, No. 6, 2023, p. 065204.

[46] Lafleur, T., Baalrud, S., and Chabert, P., "Theory for the anomalous electron transport in Hall effect thrusters. II. Kinetic model," *Physics of Plasmas*, Vol. 23, No. 5, 2016.

[47] Boeuf, J.-P., and Garrigues, L., "E× B electron drift instability in Hall thrusters: Particle-in-cell simulations vs. theory," *Physics of Plasmas*, Vol. 25, No. 6, 2018.

[48] Livadiotis, G., and McComas, D. J., "Connection between Polytropic Index and Heating," *The Astrophysical Journal*, Vol. 956, No. 2, 2023, p. 88.

[49] Vinci, A. E., Delavière–Delion, Q., and Mazouffre, S., "Electron thermodynamics along magnetic nozzle lines in a helicon plasma," *Journal of Electric Propulsion*, Vol. 1, No. 1, 2022, p. 4.

[50] Arber, T. D., Goffrey, T., and Ridgers, C., "Models of thermal conduction and non-local transport of relevance to space physics with insights from laser–plasma theory," *Frontiers in Astronomy and Space Sciences*, Vol. 10, 2023, p. 1155124.

[51] Bychenkov, V. Y., Rozmus, W., Tikhonchuk, V. T., and Brantov, A. V., "Nonlocal Electron Transport in a Plasma," *PH YS ICAL REVIEW LETTERS*, Vol. 75, No. 24, 1995.

[52] Brantov, A. V., and Bychenkov, V. Y., "Nonlocal transport in hot plasma. Part I," *Plasma Physics Reports*, Vol. 39, No. 9, 2013, pp. 698–744.

[53] Luciani, J. F., Mora, P., and Virmont, J., "Nonlocal Heat Transport Due to Steep Temperature Gradients," *Physical Review Letters*, Vol. 51, No. 18, 1983, pp. 1664–1667.

[54] Landi, S., Matteini, L., and Pantellini, F., "ELECTRON HEAT FLUX IN THE SOLAR WIND: ARE WE OBSERVING THE COLLISIONAL LIMIT IN THE 1 AU DATA?" *The Astrophysical Journal*, Vol. 790, No. 1, 2014, p. L12.

[55] Ciraolo, G., Bufferand, H., Di Cintio, P., Ghendrih, P., Lepri, S., Livi, R., Marandet, Y., Serre, E., Tamain, P., and Valentinuzzi, M., "Fluid and kinetic modelling for non-local heat transport in magnetic fusion devices," *Contributions to Plasma Physics*, Vol. 58, No. 6-8, 2018, pp. 457–464.

[56] Fundamenski, W., "Parallel heat flux limits in the tokamak scrape-off layer," *Plasma Physics and Controlled Fusion*, Vol. 47, No. 11, 2005, pp. R163–R208.

[57] Hoffman, M. D., Gelman, A., et al., "The No-U-Turn sampler: adaptively setting path lengths in Hamiltonian Monte Carlo." *J. Mach. Learn. Res.*, Vol. 15, No. 1, 2014, pp. 1593–1623.